The DNA–Carbon Nanotube Binding Mode Determines the Efficiency of Carbon Nanotube-Mediated DNA Delivery to Intact Plants

*Zahir Ali[1,∞], Maged F. Serag[2,∞], Gozde S. Demirer[3, $], Bruno Torre[4, 5, #], Enzo di Fabrizio[4, 5, 6], Markita P. Landry[3], Satoshi Habuchi[2, *], and Magdy Mahfouz[1, *]*

[1] Laboratory for Genome Engineering and Synthetic Biology, Division of Biological Sciences, 4700 King Abdullah University of Science and Technology, Thuwal 23955-6900, Saudi Arabia.

[2] King Abdullah University of Science and Technology (KAUST), Biological and Environmental Sciences and Engineering Division, Thuwal 23955-6900, Saudi Arabia.

[3] Department of Chemical and Biomolecular Engineering, University of California Berkeley, Berkeley, CA, USA.

[4] SMILEs Lab, Physical Science and Engineering (PSE) and Biological and Environmental Science and Engineering (BESE) Divisions, King Abdullah University of Science and Technology, Thuwal 23955-6900, Saudi Arabia.

[5] High-Speed Fluids Imaging Lab, Physical Science and Engineering (PSE) Division, King Abdullah University of Science and Technology, Thuwal 23955-6900, Saudi Arabia.

[6] Materials and Microsystems Laboratory, Department of Applied Science and Technology, Politecnico di Torino, 10129 Torino, Italy.

[∞] These authors contributed equally to this work

[*] Correspondence should be addressed to Magdy Mahfouz (magdy.mahfouz@kaust.edu.sa) and Satoshi Habuchi (Satoshi.Habuchi@kaust.edu.sa)

[$] Current address: Department of Plant Biology and Genome Center, University of California, Davis, 451 Health Sciences Drive, Davis, CA 95616, USA

[#] Current address: Department of Applied Science and Technology (DISAT), Polytechnic of Turin, Corso Duca degli Abruzzi 24, 10129, Torino, Italy

Supporting Text

1. Detection of binding modes of DNA

The inherent limitations of low throughput and the slow scanning speed render AFM as single molecule/single particle analysis technique rather than a batch or ensemble average analytical technique. The resolution is another limiting factor in our experiments. In general, increasing the scan size usually comes with limited resolution that affect the proper judgement on the acquired images. Although increasing the scan size in homogenous samples of ultra-high purity such as metallic nano-rods is helpful to increase the analytical throughput of AFM, our sample is highly heterogeneous with fragment sizes of SWCNTs and carbonaceous fragments reacted with PEI ranging between a sub-nanometer to few micrometers. The yellow arrows in Fig. ST1 point to spatially isolated sub-micrometer size fragments, whereas the red arrows point to fragments with similar size that are close or attached to the carbon nanotubes. Therefore, it is difficult to reliably discern whether these structures (red arrows) are artifacts (i.e., fragments of SWCNTs and carbonaceous fragments reacted with PEI) or DNA molecules based on AFM images obtained with large scan fields.

To overcome the above challenges, we first acquired AFM images with large scan fields (Fig. ST1a-d). Then, we zoomed-in around SWCNTs that are located close (or attached) to the fragments, such as the areas marked with red arrows. In the zoomed images, artifacts (i.e., fragments of SWCNTs and carbonaceous fragments reacted with PEI) appear featureless (blue arrows in Fig. ST1e) whereas DNA have featured structures (see Fig. ST1f white arrow). It is important to underline that these featured structures (DNA) are absent in the control samples (PEI-SWCNT).

To verify that our observations of the DNA condensation modes are not due to the presence of artifacts, we performed a symmetry analysis of the structures in both the control samples and the DNA-PEI-SWCNT samples (Figs. ST2 and ST3). We note that the deposition of PEI onto small carbonaceous / SWCNTs fragments resulted in structures that are symmetric along their full line of symmetry (Inset of figure ST2-A and Fig. ST2-G). On the other hand, the condensation of DNA resulted in structures that are symmetric along the upper half of its height, yet largely asymmetric along their lower half (Inset of Fig. ST2-E and Fig. ST-H). We analyzed the structures appearing in the AFM images of the control (PEI-SWCNT) and DNA (DNA-PEI-SWCNT) samples at different scan sizes (magnifications) where we normalized their heights between 0 and 1. Next, we aligned the lateral axes of the structures such that their lines of symmetry lie at 0 nm (Fig. ST3-A,B), where the values to the right and to left sides of the axes have negative and positive signs, respectively. The symmetry of structures was thus defined as the fluctuations of their lateral axis on both sides of their line of symmetry at the same height and was calculated by summation of the lateral axes values on both sides of the symmetry line (positive values added to the negative values) at each height value. Thus, the feature tends to be symmetric when its symmetry value approaches zero (i.e., the features that exist at the upper half height of the artifacts and the condensed DNA structures), whereas the feature is largely asymmetric when its symmetry value largely deviates from zero (i.e., features that exist at the lower half of the height of the condensed DNA structures) (Fig. ST3-C). To assess the contribution of artifacts in our AFM results, we note that the absolute symmetry values (calculated at the lower half of the height) of our AFM images showing condensed DNA are more than or equal to 25 (the symmetry regime highlighted in cyan in Fig. S3-D). Only 13% of the symmetry values in this symmetry regime corresponds to artifacts. Thus, in every 10 representative AFM images of condensed DNA structures (for example those shown

for condensed and partially condensed DNA in Supplementary Appendix 2) we have approximately one artifact structure. Taken together, the contribution of artifacts in our AFM images and in our results remains very low, which has a negligible effect on the conclusions of this study.

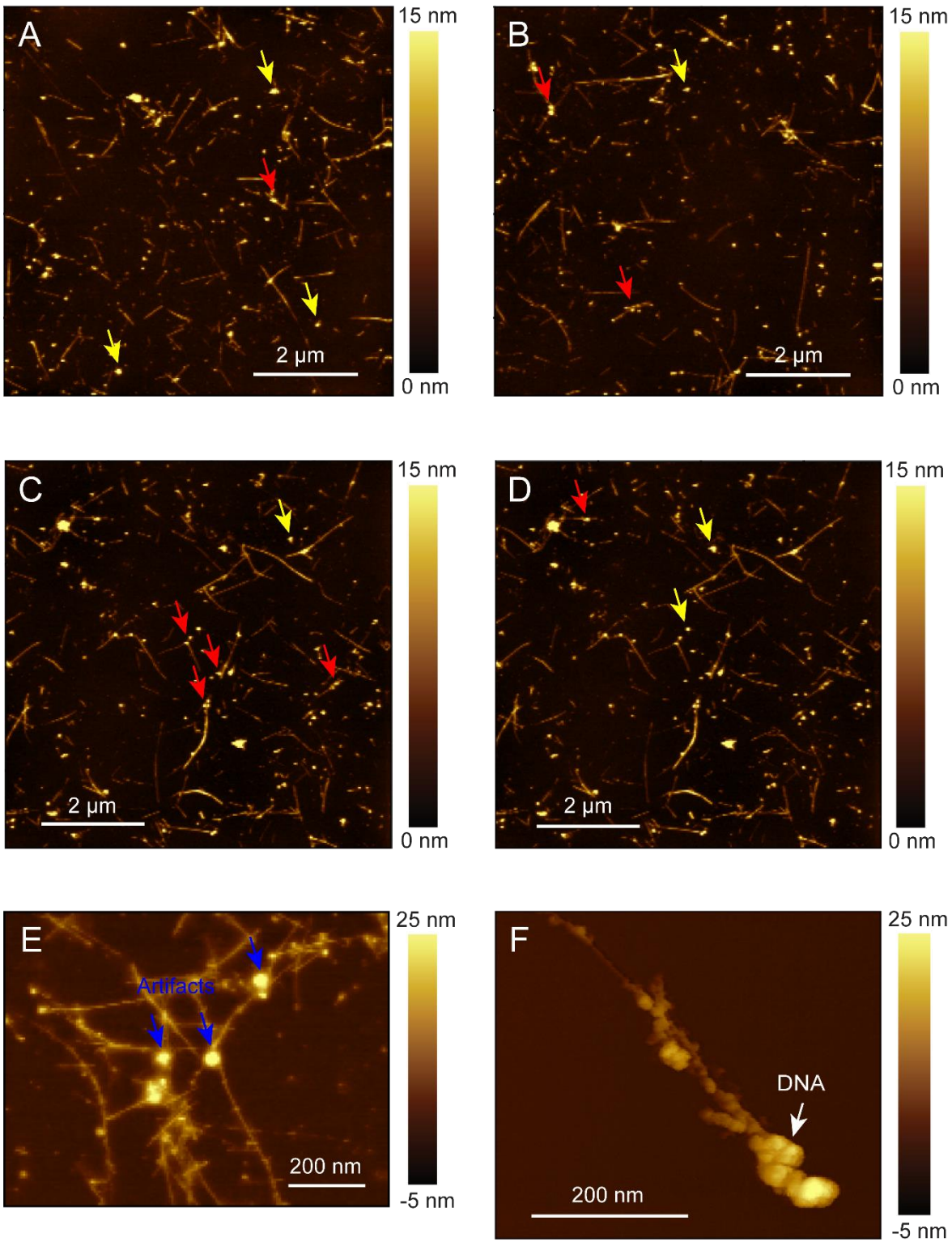

Fig. ST1. Detection of DNA binding to PEI-SWCNT. a) – d) AFM topographic wide scan fields. The red arrows indicate fragments that are close or attached to PEI-SWCNT, whereas the yellow

arrows indicate fragments that are scattered and abundant in the scanning field. e) Enlarged view of the artifacts. f) Enlarged field of DNA attached to PEI-SWCNTs.

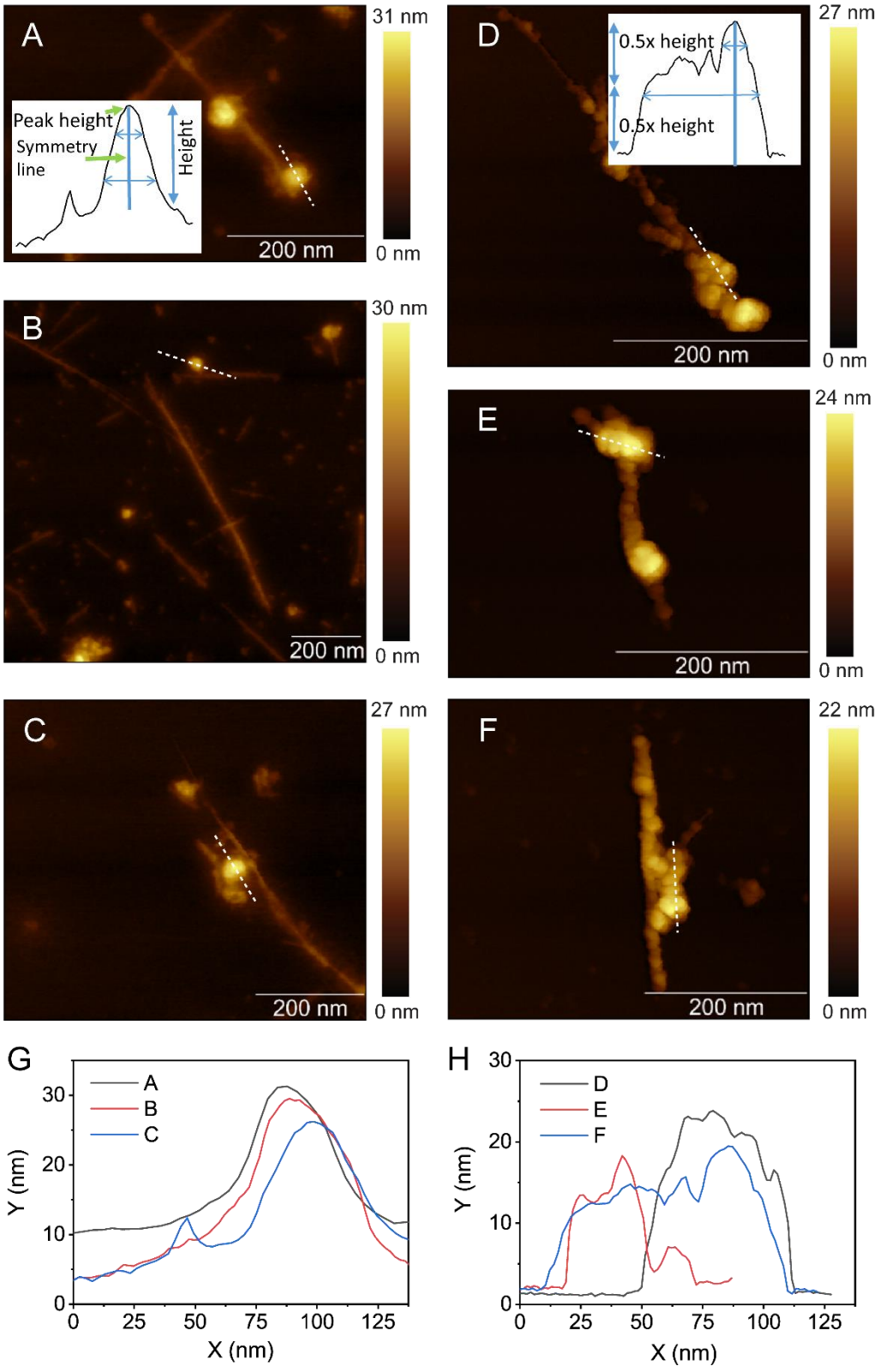

Fig. ST2. Symmetry of the artifacts structures and the condensed DNA A) – C) AFM topographic images of the artifacts structures in the PEI_{30}-SWCNT control samples. The inset of figure A shows the peak point of the height of the artifacts (peak height) which we used to draw the line of symmetry (symmetry line). E) – F) AFM topographic images of the condensed DNA structures in the DNA-PEI_{30}-SWCNT samples. The inset of figure D shows the features are symmetric relative to the line of symmetry in the upper half of the height, yet largely asymmetric in the lower half of the height. G) and H) The height profiles of the structures shown in the AFM images in figures A – E.

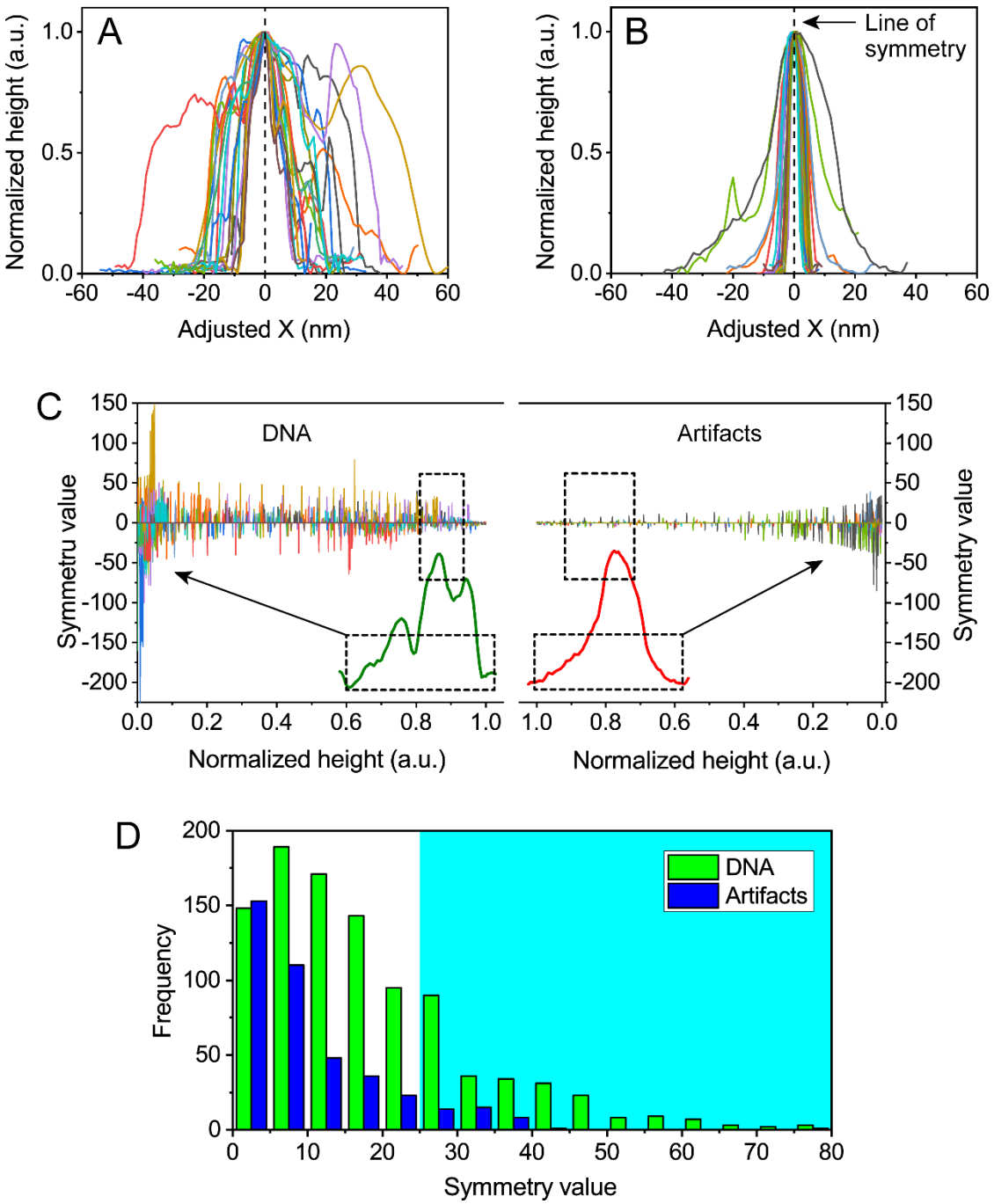

Fig. ST3. Symmetry analysis of the artifacts structures and the condensed DNA A) and B) The normalized height profile of the DNA (A) and the artifacts (B) structures. The lines of symmetry were aligned at lateral value of 0 nm. C) The symmetry values (Y axis) at each value of normalized height (X axis) of the DNA and artifacts structure. D) Frequency distribution of the

absolute symmetry values shown in C for DNA and artifacts. The cyan shading highlight the symmetry regime where the contribution of artifacts is minimal.

2. Detection level sensitivity of western blotting

We used confocal fluorescence microscopy (that detects fluorescence emitted by expressed proteins (GFP in this study)), RT-qPCR (that amplifies the nucleic acid signal), and western blot (that detects the original molecules of proteins without amplification) to confirm the expression of GFP. Western blot detection level is not as sensitive as confocal fluorescence microscopy and RT-qPCR in the detection of the expression, and thus, cannot detect very low level of expression of GFP obtained by infiltrating plasmid DNA using the PEI_{30}-SWCNT-DNA complex (i.e., 0.09% efficiency compared with *Agrobacterium*-infiltrated leaves).

3. Employment of Dynamic light scattering to measure the experimental hydrodynamic diameter of carbon nanotubes

The basic principle of dynamic light scattering (DLS) is the ability of particles to scatter light in elastic manner (regardless the shape), where big particles scatter much more light compared with smaller particles. SWCNTs are high aspect ratio structures and therefore we did not use the measured hydrodynamic diameters to refer to any physical characteristics of the nanotubes. We used the numbers just to indicate whether the sample has aggregates or not. This approach is valid based on the principle of elastic light scattering.

It is important to note that the measured zeta potential of SWCNTs is based on light scattering where the mathematical formulas are developed assuming spherical particles surrounded by ion layers. We and others have used the zeta potential as numbers to differentiate between SWCNT-

COOH and SWCNT-PEI. While doing this, the shape of SWCNT is approximated as spherical particles. As such, the use of DLS to probe the presence of aggregation of SWCNTs is a valid approach. Our AFM data in Fig. ST5 support the dynamic light scattering data shown in Fig. 3 and confirm this validity.

4. Physical characteristics of PEI and chitosan

We outline two important terms that are essential to understand the physical difference between PEI and chitosan.

Bjerrum length (l_B): is the distance at which the electrostatic potential (E) between two similarly charged particles is equal to the thermal energy (k_BT; where k_B is Boltzmann constant and T is the absolute temperature; see the schematic below). For example, the Bjerrum length of water is 0.71 nm. This means that when the distance between two water molecules is greater than 0.71 nm, the coulomb interaction (repulsion or attraction) is insignificant compared to the thermal energy.

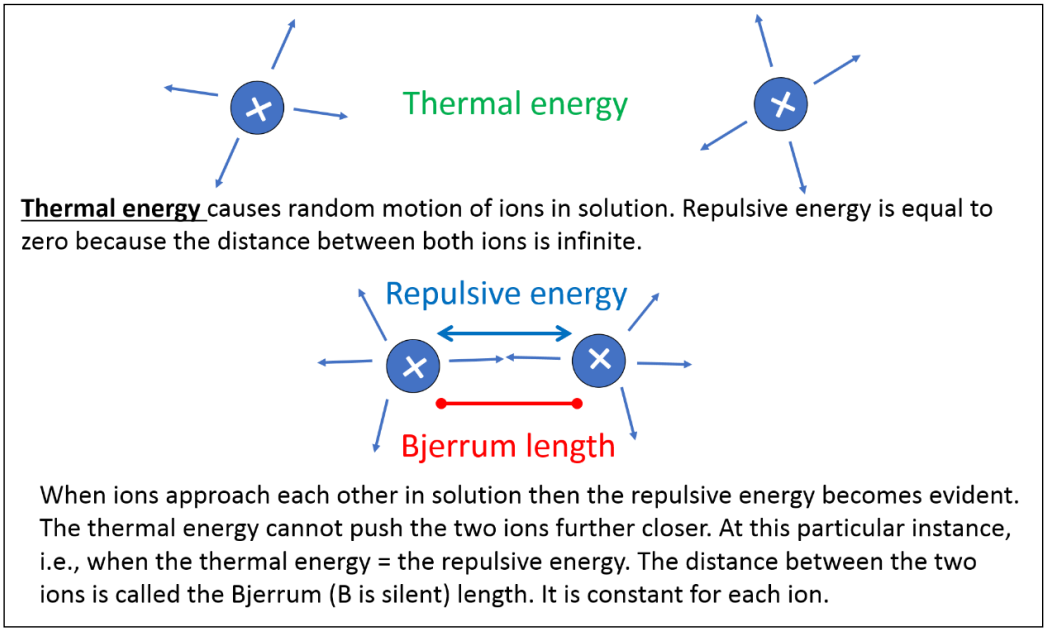

Debye length (l_D): is the thickness of the double layer (The stern layer (counterions) and the less tightly held diffuse layer (multilayers of co-ions)) that form at a charged surface (see the schematic below). This length is also known the shielding distance: distance over which the charged surface is shielded from the bulk solution (see Fig. ST4). If the ionic strength is increased, the shielding will be higher (short Debye length) and vice versa.

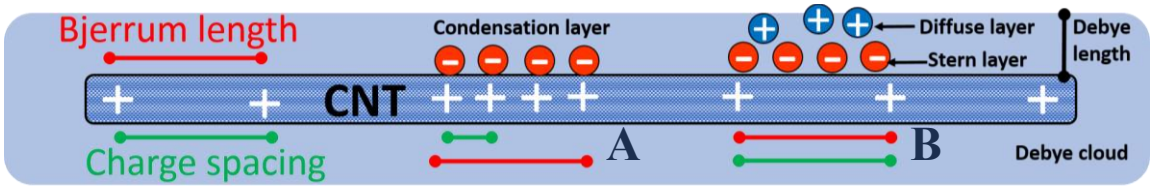

Figure ST4. A Schematic drawing illustrating the concept of Bjerrum length and Deby length. A condensation layer is formed at the surface of highly charged rod-like polymers (region A) whereas the typical stern and diffuse layers are formed at the surface of moderately charged polymers (region B).

Table ST1: Physical and chemical characteristic of PEI and chitosan.

Physicochemical characteristic	PEI	Chitosan
Chemical structure	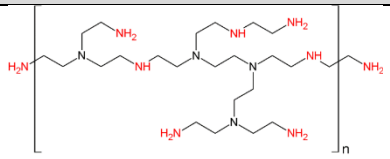	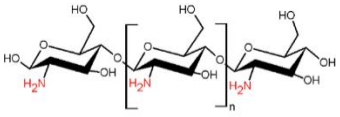
Molecular weight	25,000 Da	50,000 – 190,000 Da
pKa	7.11 – 8.6[a]	6.5
Basic amino groups per a monomer	4 (primary), 2 (secondary) and 3 (tertiary)[b]	1 (primary)[b]
Repeat units	50 mer	225 – 825 mer

Radius of gyration (R_g)	17 nm	60-160 nm[c]
R_g at 50% ionization of the NH_2 groups	27 nm[d]	–
Average intramolecular distance between the amino groups	0.28 nm[e]	0.6 nm[e]
Bjerrum length	17 nm[f]	1.5 nm[f]

[a] The values are dependent on molecular weight and degree of branching. The p*K*a values imply higher basic characteristics of PEI and hence PEI is easier to get protonated (more basic).

[b] PEI has much bigger number of basic amino groups, and hence has much higher positive charge per one monomer, than chitosan.

[c] The radius of gyration of chitosan vary based on pH and degree of acetylation.

[d] The radius of gyration shows this increase due to the intramolecular charge repulsion and hence charge separation increases.

[e] The value of PEI was calculated based on the closest distance between the primary and secondary amino groups in one monomer, whereas the value of chitosan was calculated based on the distance between two amino groups in neighboring monomers.

[f] The Bjerrum l_B length of chitosan and PEI at RT can be calculated from the equation: $l_B = \frac{q^2}{4\pi\varepsilon_\circ\varepsilon K_B T}$, where q is the elementary charge, ε_0 is the vacuum permittivity, ε is dielectric constant, K_B is Boltzmann constant and T is the absolute temperature. The dielectric constant of PEI is 3.3, whereas the dielectric constant of commercial partially deacetylated chitosan is 37. The value of deacetylated chitosan which we used to coat CNT should be slightly bigger than this value due to the presence of more free amino groups, but it is still smaller than that of PEI).

From the above table we note that the physicochemical characteristics (molecular size, p*K*a, number of bare charges, intramolecular charge separation and the Bjerrum length) renders CNT-PEI a highly charged rod-like polyelectrolytes (high charge density on a smaller sized polymer) and renders the CNT-chitosan a moderately charged rod-like polyelectrolyte (lower charge density on bigger sized polymer).

To illustrate the effect of this difference in charge density between PEI and chitosan, we note that if charged polymers such as PEI and chitosan are covalently bound to a 1D surface such as a

single walled carbon nanotube, we would have a configuration like what is shown in the schematic shown in Fig. ST4. In region B of the schematic, the surface is moderately charged (polymers with Bjerrum length comparable to charge spacing such as chitosan, see Table ST1). This creates double layer of ions in solution where an initial layer of counterions bind to the surface followed by a diffusive layer of co-ions. On the other hand, in region A, the surface is highly charged (polymers with longer Bjerrum length comparable to charge spacing such as PEI, see Table ST1). This high charge causes the counterions to condense (much more strongly held) on the surface until the high charge is partially neutralized so that the Bjerrum length and charge spacing become equal (l_B/l = 1, called charge renomalization). In other word, counterion condensation on polyelectrolytes occurs when the linear bare charge density of polyelectrolytes exceeds a threshold value (the l_B/l ratio is greater than 1). The ratio l_B/l = 1 (where electrostatic repulsion is equal to thermal energy) is restored once the counterions are condensed. The thickness of the condensed layer of ions varies based on the linear charge density. These layer(s) are strongly held, highly ordered, compact layer(s) (C.F. the stern layer) onto the polyelectrolyte and is viewed as a part of its structure (C.F. the stern layer in the case of moderately charged surfaces).[1] However, in the case of less positive charge (but the l_B/l is still greater than 1), only part of DNA is condensed which is enough to restore the ratio to 1 (viewed as part of the structure of the linear rod-like structure), whereas the remaining part stays loosely bound. This loosely bound DNA is the accessible part to the transcription machinery of the cell.

The differences in the thickness between the condensed layer (in case of PEI) and the diffuse layer in case of chitosan explains why the measured hydrodynamic diameter of PEI-SWCNTs is larger than that of chitosan-SWCNTs.

The presence of aggregates in the solution of PEI-SWCNTs but not in the solution of chitosan-SWCNTs (Fig. ST5) can be explained within the framework of the theory of counterion condensation and like-charge attraction. The theory states that attraction between two highly charged rod-like polymers where $l_B/l > 1$ occurs if the salt concentration c is low enough to satisfy $l_D >> r$, where $l_D = (8\pi l_B c)^{-1/2}$ and r is the polyelectrolyte radius. Having r = 2.5 nm (AFM height of PEI-SWCNTs is 5 nm), the salt concentration for efficient ion condensation is 10 μM (l_D=15 nm) or lower. Therefore, the linear polyelectrolyte traps the trace ions in the solution and condenses them on its surface. Concentrations above this value would cause counterion-condensation weaker and hence cause the like-charge attraction to gradually weaken until the attraction force reaches zero at very high salt concentration (where the screening length is equal to 0 (l_D=0)). Note that we add DNA gradually to carbon nanotubes so highly charged molecules like DNA co-condense with ions on the surface of CNT-PEI.

To explain the physical reason of this like-charge attraction, we note that at intermediate range of distances between two polyelectrolytes (less than the screening length), each charged rod-like polyelectrolyte becomes inside the Debye cloud of the other but still partially screened from one another. Therefore, the attraction between the two rod-like electrolytes can theoretically happen within a distance of 70 nm (one order of magnitude bigger than the diameter of CNT-PEI, at 0.5 μM ionic strength), within a distance of 15 nm (at 10 μM ionic strength) or within distance of 1 nm (at 1 mM ionic strength). These shorter distances can be reached during crowding in concentrated solutions and under shear conditions. As the two polyelectrolytes approach each other within these distances, the condensation volume increases (thickness of the condensed layers, i.e., the layer become less ordered and less condensed) by two orders of magnitudes[1] due the mutual polarization of each polyelectrolyte by the other. This increase in the condensation volume

(randomization of the ions within the layers and conversion from ordered to less ordered state) results in an increase in the entropy of the condensed counterions leading eventually to strong attraction between the two likely charged rod-like polyelectrolytes (CNT-PEI).

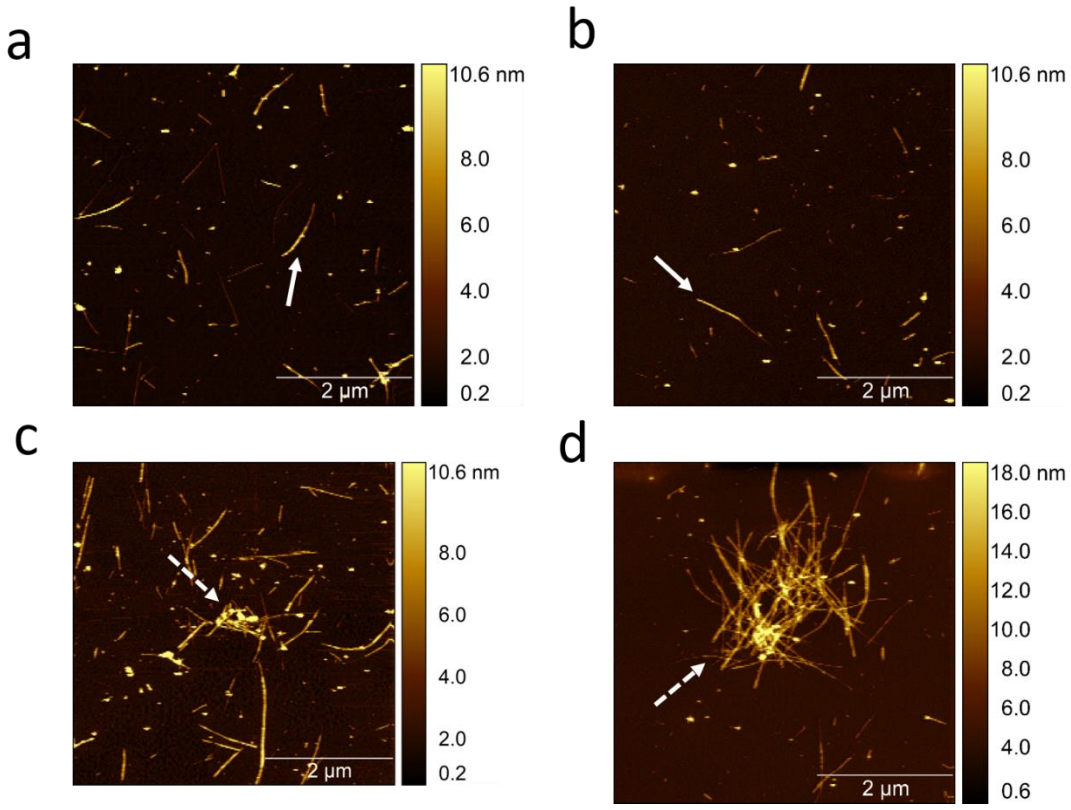

Figure ST5. Aggregation of polymer coated SWCNT. a) Dry-phase AFM topographic image of freshly sonicated chitosan-SWCNTs. The dispersion is stable where the nanotubes did not show any aggregation by incubation for several days. The white arrow indicate isolated SWCNT. b) Dry-phase AFM topographic image of freshly sonicated PEI-SWCNTs. The white arrow indicate isolated SWCNT. c) Dry-phase AFM topographic image of PEI-SWCNTs incubated for 24 at RT. The dashed arrows indicate aggregated SWCNTs. d) Dry-phase AFM topographic image of PEI-SWCNTs incubated for 48 at RT. The dashed arrows indicate aggregated SWCNTs.

5. Batch-to-batch variation of the synthesized PEI-SWCNT

We note that we synthesized several batches of each PEI_{xx}-$SWCNT^{xxmV}$ material and did a comprehensive characterization of each batch. We observed large batch-to-batch variations in terms of the measured zeta potential. Even with PEI_{30}-SWCNT that often gave us positive transformation results, some batches showed zeta potential below 60 mV. These batches resulted in negative transformation. This could be due to minor variations in the room temperature during overnight incubation and/or pipetting errors. That's why we noted the measured zeta potential with each preparations (e.g. PEI_{20}-$SWCNT^{+52mV}$, PEI_{30}-$SWCNT^{+55mV}$, and PEI_{30}-$SWCNT^{+61mV}$) and used this notation to refer to specific results. Therefore, it is hard to predict the zeta potential value that can be obtained from a specific PEI-SWCNT conjugate until we measure the zeta potential after synthesis. The zeta potential of PEI-SWCNT conjugates generated after 12 h of incubation (e.g. PEI_{20}-$SWCNT^{+52mV}$) and that of conjugates showing unexpected zeta potential value (e.g. PEI_{30}-$SWCNT^{<+61mV}$) range between 50mV and up to 60mV. These preparations did not show GFP expression.

6. Relationship between the charge density along the PEI-SWCNTs and the binding mode of the plasmid DNA

We were not able to assign a specific mode of binding to a specific range of local surface potentials using KPFM for the following reasons. 1) Based on the counter-ion condensation theory (reference 43), the condensed counterions (DNA in our experiment) are viewed as part of the structure of the rod-like polyelectrolyte (PEI-SWCNT) as if it is covalently bound. Therefore, once DNA binds to PEI-SWCNT, the local charged zones on the PEI-SWCNT are not accessible by the

conductive probe in KPFM. 2) The condensation of DNA on SWCNT-PEI occurs when the linear bare charge density of the polyelectrolyte (PEI-SWCNT) exceeds the threshold value (the l_B/l ratio is greater than 1). The ratio l_B/l = 1 (where electrostatic repulsion is equal to thermal energy) is restored once the counterions (DNA) are condensed. Thus, the degree of DNA condensation (i.e. the part of DNA involved) depends on the linear charge density of each PEI-SWCNT. This means that in the case of extreme positive charge, the DNA is fully condensed to restore the ratio l_B/l to the unity value. However, in the case of less positive charge (but the l_B/l is still greater than 1), only part of DNA is condensed which is enough to restore the ratio to 1 (viewed as part of the structure of the linear rod-like structure), whereas the remaining part stays loosely bound. This loosely bound DNA is the accessible part to the transcription machinery of the cell and to the conductive probe. Thus, this configuration would give a negative and, or misleading values of the underlying positive charge. 3) The fact that we observed the condensed and partially condensed DNA in the samples with high zeta potential (ζ = +61 - +77 mV) but not in the samples with lower zeta potential (ζ < +61 mV) suggests a link between the synthesis of highly charge material and the formation of condensed and partially condensed forms. Thus, we posited a similar link between the local zones of high positive charge and the formation of condensed and partially condensed DNA.

Supporting Figures

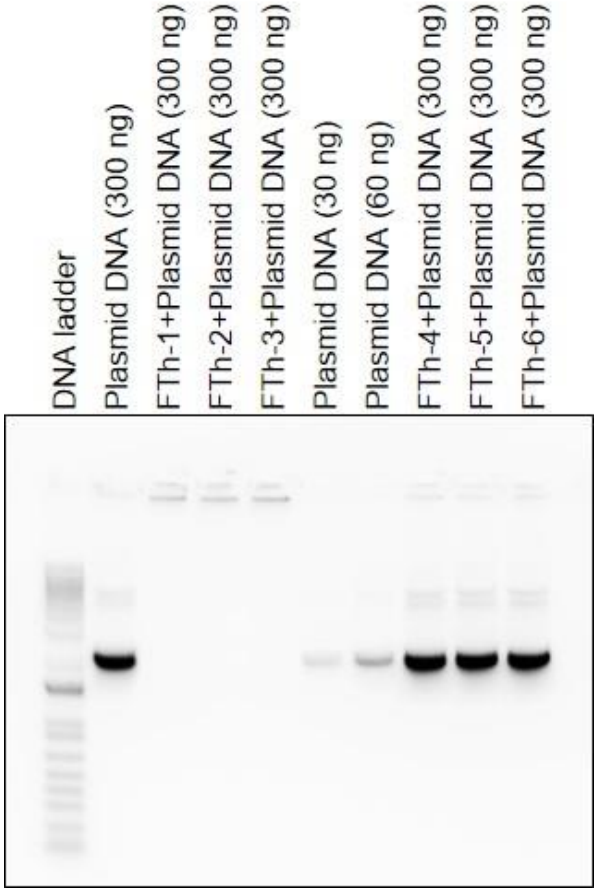

Figure S1. Removal of excess PEI after conjugation with SWCNT. PEI-SWCNT (ratio = 30 mg : 1 mg) was washed several times with water to remove excess PEI. Flow through (FTh) was collected from each filtration step and 50 µl of the filtration flow-through is mixed with 300 ng of DNA. The DNA-PEI complexes were separated on agarose gel, where retention of DNA represents free PEI polymer in the flow-through. Plasmid DNA (300 ng, 30 ng and 60 ng) were used as control for DNA retention.

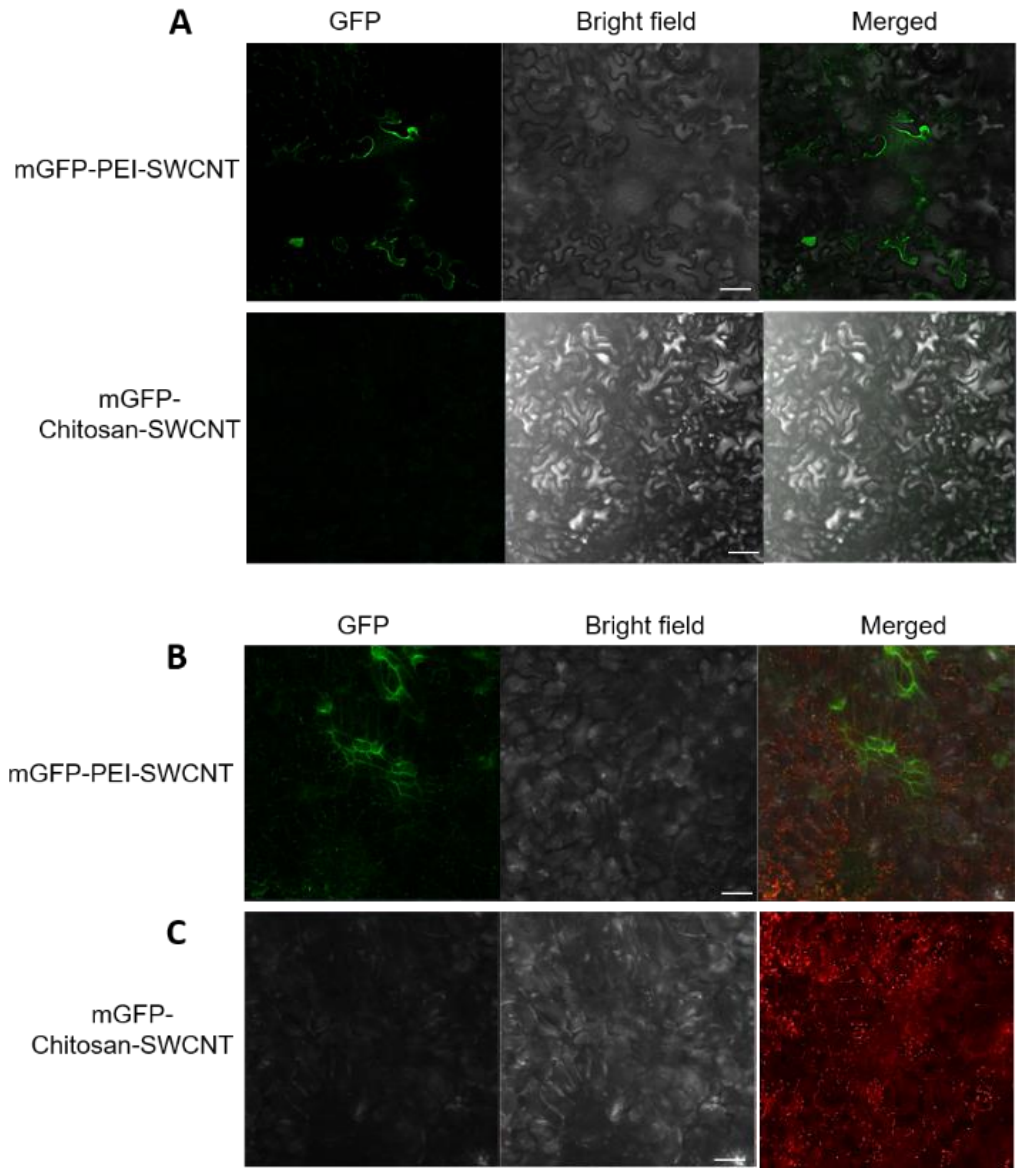

Figure S2. Confocal microscope images of the leaves infiltrated with the mGFP (4.2kb plasmid)-PEI-SWCNT. mGFP-PEI_{30}-SWCNT was infiltrated to *N. benthamiana* leaves and cotton cotyledonary leaves. The infiltrated leaves were subjected to confocal microscopy after 3 days of infiltration. Confocal images are of A) *N. benthamiana*, B) cotton cotyledonary leaves and C) control cotton cotyledonary leaves. All images are of 20x magnification, scale bar 100 µm.

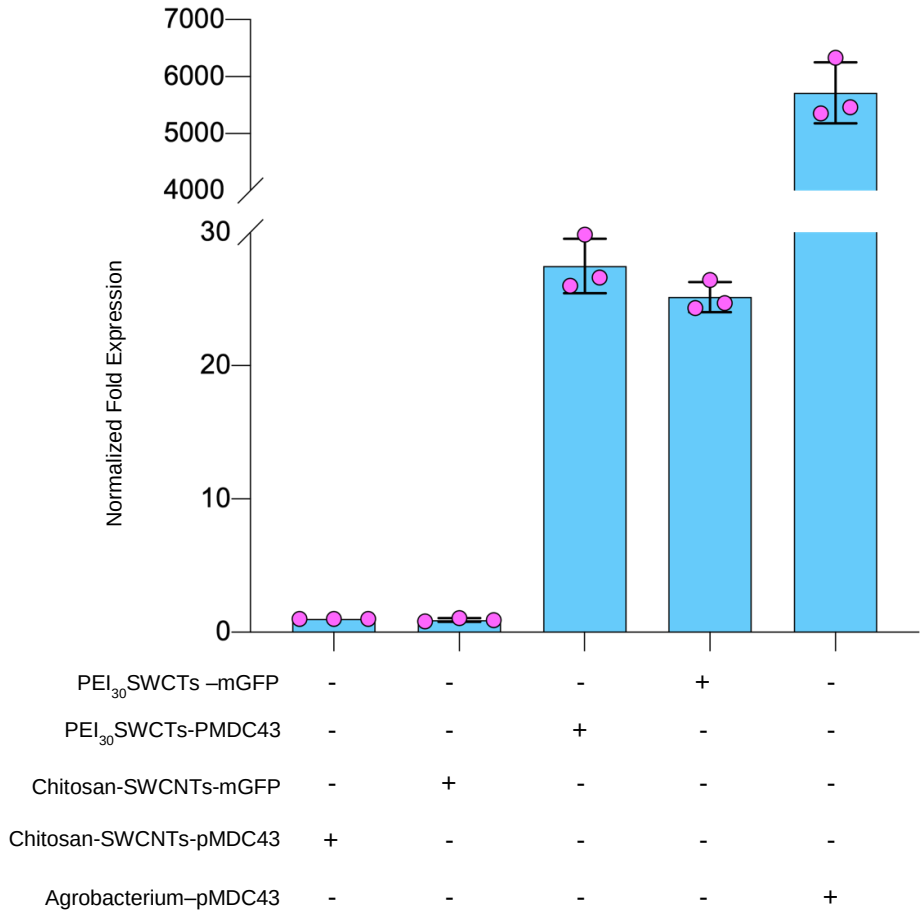

Figure S3. GFP expression quantification. mGFP (4.2 kb plasmid) and pMDC43 (10.6 kb) binary vector with GFP expression cassette) plasmid DNA were complexed with PEI_{30}-SWCNTs in MES infiltration buffer and infiltrated into the leaves of three weeks old *N. benthamiana* plants. RNA was purified three days after infiltration, treated with DNase I and subjected to one-step RT-qPCR. Plasmid complexed with Chitosan-SWCNTs and *Agrobacterium* containing the pMDC43 were used as experimental controls. *N. benthamiana* PP2A gene was used as an expression reference. The error bar represents the standard error of the mean.

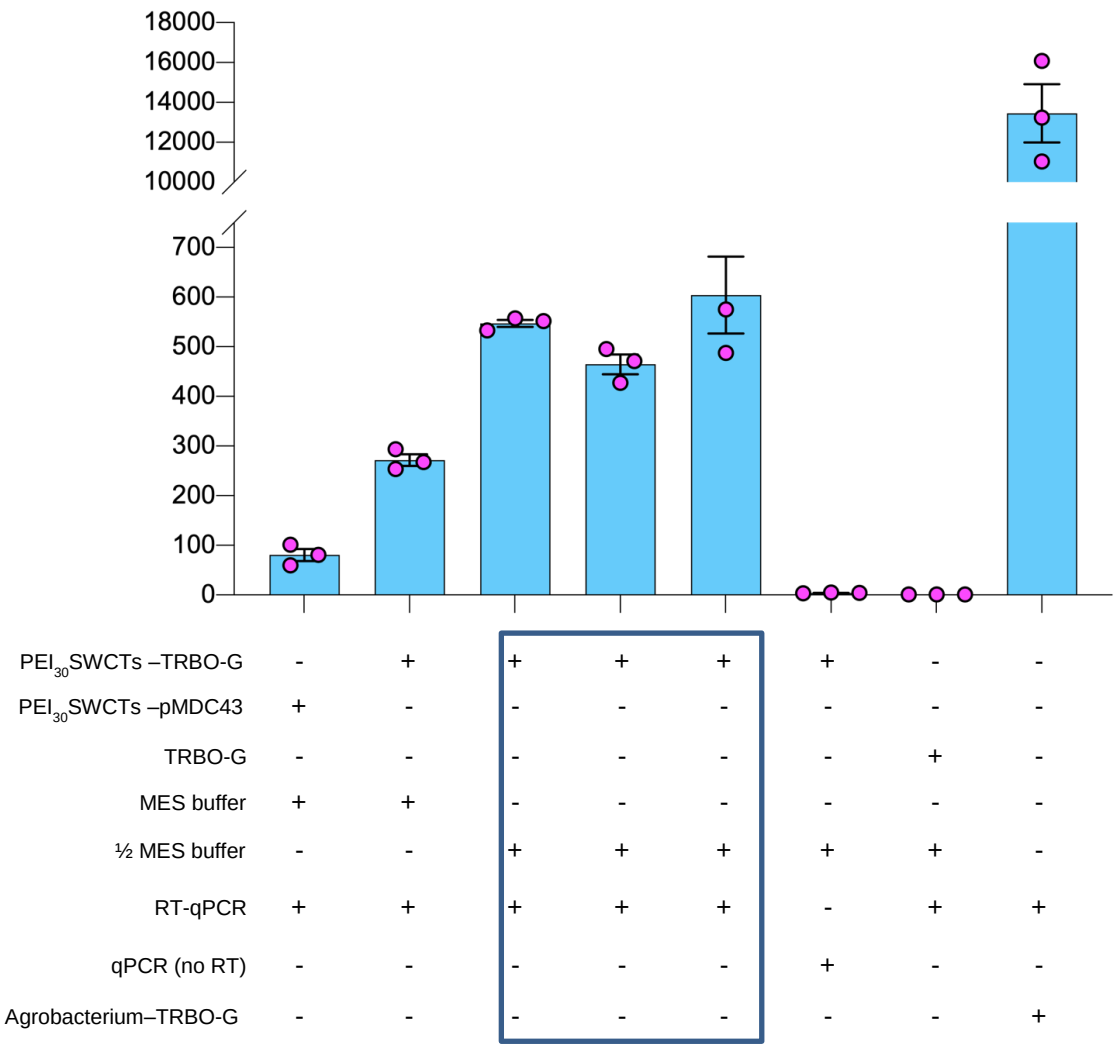

Figure S4. GFP expression quantification. pMDC43 (binary vector with GFP expression cassette) and TRBO-G plasmid DNA were complexed with PEI_{30}-SWCNTs in MES and ½ MES infiltration buffer and infiltrated into three weeks old *N. benthamiana* plants. RNA was purified three days after infiltration, treated with DNase I and subjected to one-step RT-qPCR. TRBO-G plasmid only and Agrobacterium harboring the TRBO-G binary plasmid were used as experimental expression controls. qPCR without reverse transcriptase was used as DNA contamination control. Boxed samples are three individual plant replicates infiltrated with the same DNA-PEI_{30}-SWCNT complex. *N. benthamiana* PP2A gene was used as an expression reference. The error bar represents the standard error of the mean.

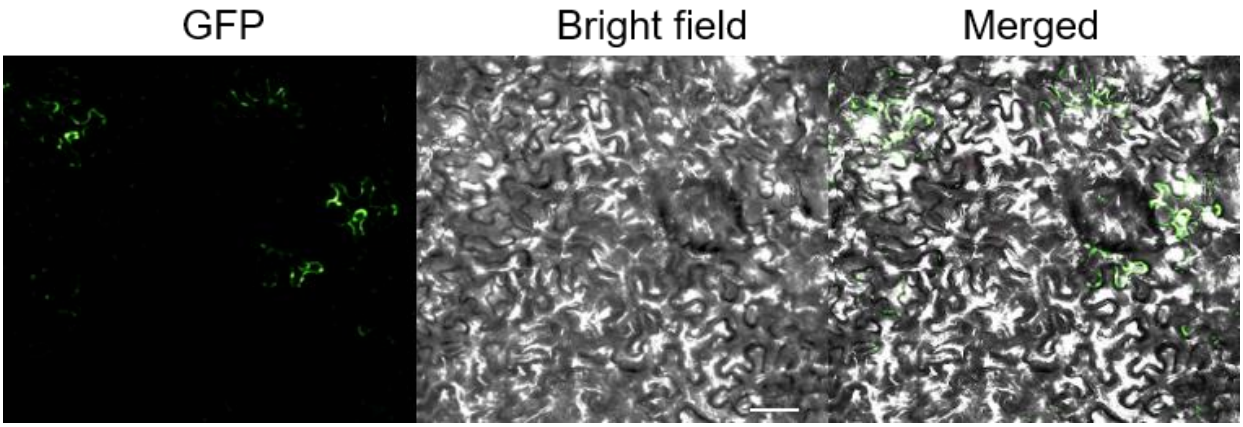

Figure S5. Confocal microscope images of the leaves infiltrated with the pMDC43-PEI-SWCNT. pMDC43-PEI_{30}-SWCNT was infiltrated to *N. benthamiana,* leaves. The infiltrated leaves were subjected to confocal microscopy after 3 days of infiltration. All images are of 20x magnification, scale bar 100 μm.

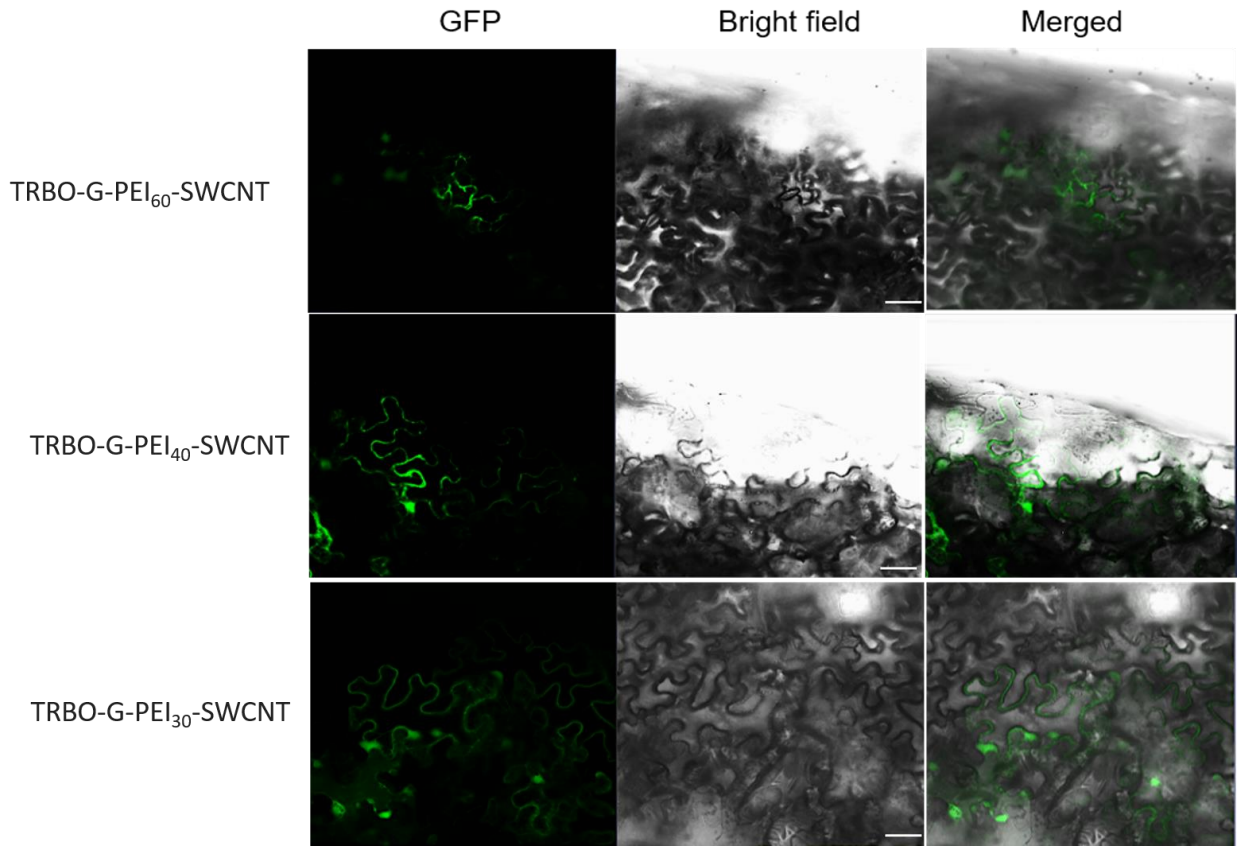

Figure S6. Confocal microscope images of the leaves infiltrated with the TRBO-G-PEI-SWCNT. TRBO-G-PEI_{30}-SWCNT, TRBO-G-PEI_{40}-SWCNT and TRBO-G-PEI_{60}-SWCNT were infiltrated to *N. benthamiana* leaves. The infiltrated leaves were subjected to confocal microscopy after 3 days of infiltration. Tissue damage in the leaves infiltrated with high PEI concentrations (TRBO-G-PEI_{40}-SWCNT and TRBO-G-PEI_{60}-SWCNT) was observed as undefined structures. All images are of 20x magnification, scale bar 100 μm.

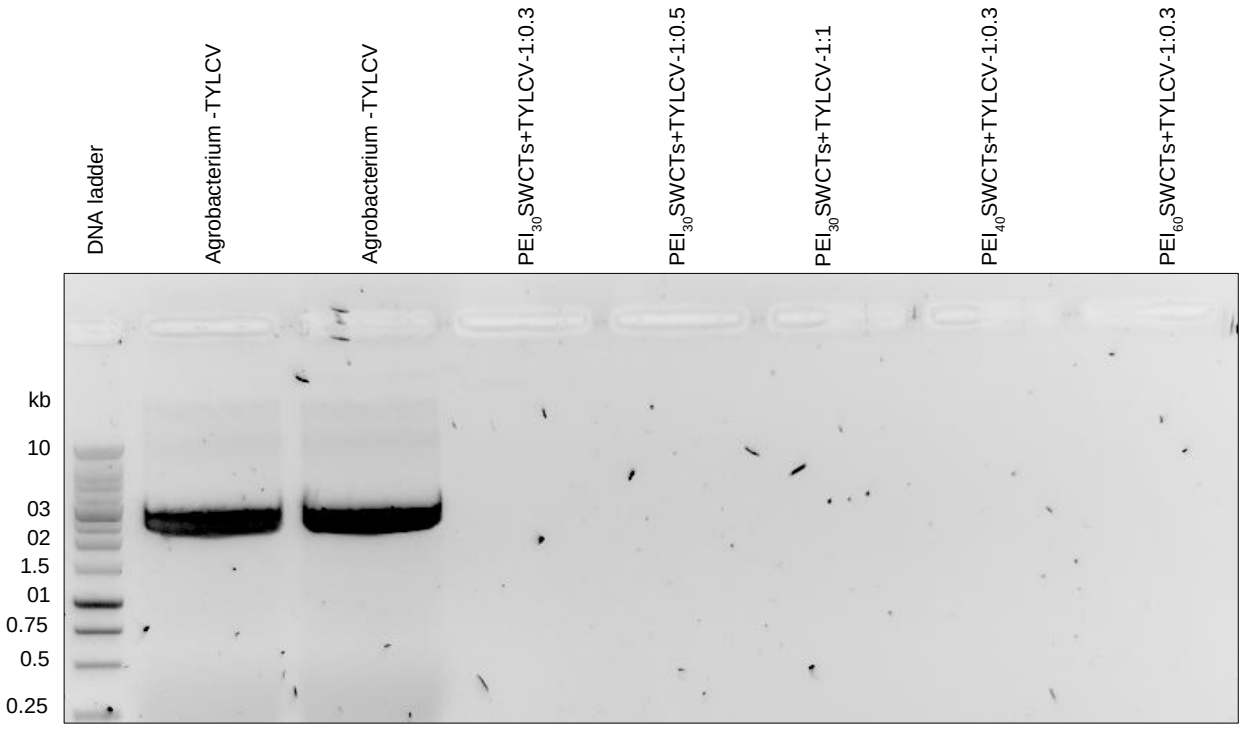

Figure S7. Rolling Circle Amplification (RCA) assay for TYCLV genome amplification. Plasmid DNA was complexed in different ratio (1:3,1:2, 1:1) with $PEI_{30/40/60}$-SWCNTs in ½ MES infiltration buffer. DNA samples extracted from three weeks old *N. benthamiana* plants were subjected to RCA. Agrobacterium containing the TYLCV genome harboring binary plasmid was used as control. Samples were collected from the young top three leaves ten days after infiltration. RCA product was separated on 1% agarose gel. 1 kb DNA ladder.

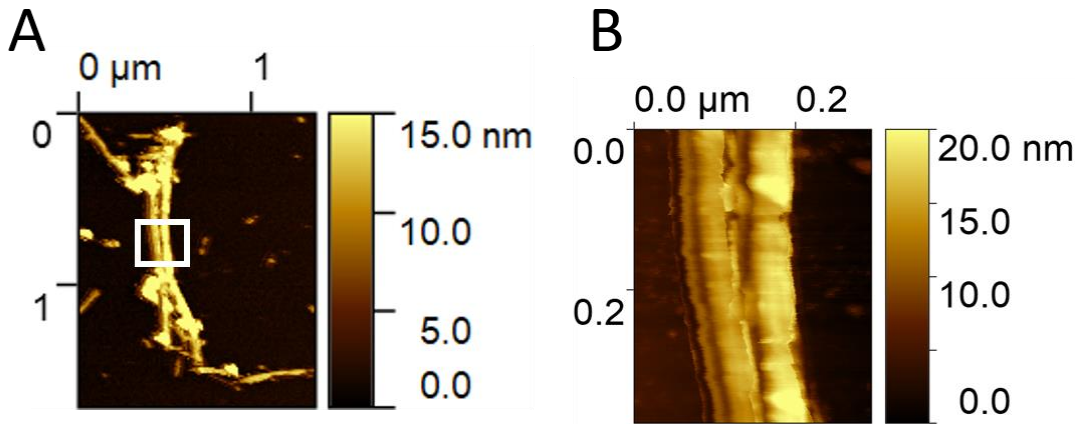

Figure S8. (A) Dry-phase AFM topographic image of PEI_{30}-SWCNT aggregated along their side walls. (B) Enlarged view of the area marked by the white square in (A).

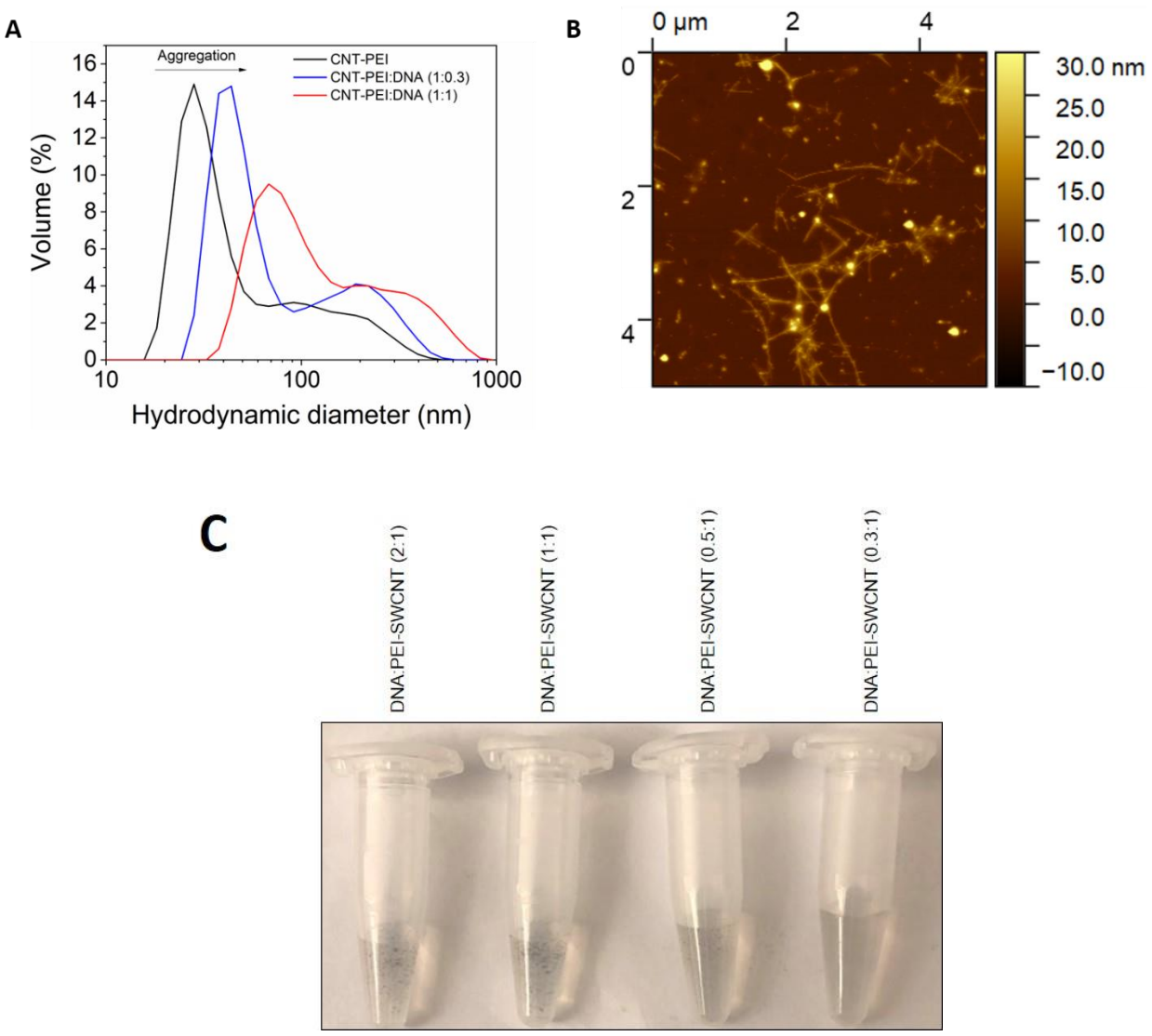

Figure S9. Aggregation of PEI_{30}-SWCNT upon complexation with DNA A) Distribution of hydrodynamic diameter of PEI_{30}-SWCNT upon addition of increasing concentrations of DNA. B) Dry-phase AFM topographic images of PEI_{30}-SWCNT complexed with DNA. C) Precipitation of PEI-SWCNT upon addition of excess DNA molecules. DNA:PEI-SWCNT ratios = 2:1, 1:1 and 0.5:1 (precipitation) versus ratio = 0.3:1 (no precipitation).

A

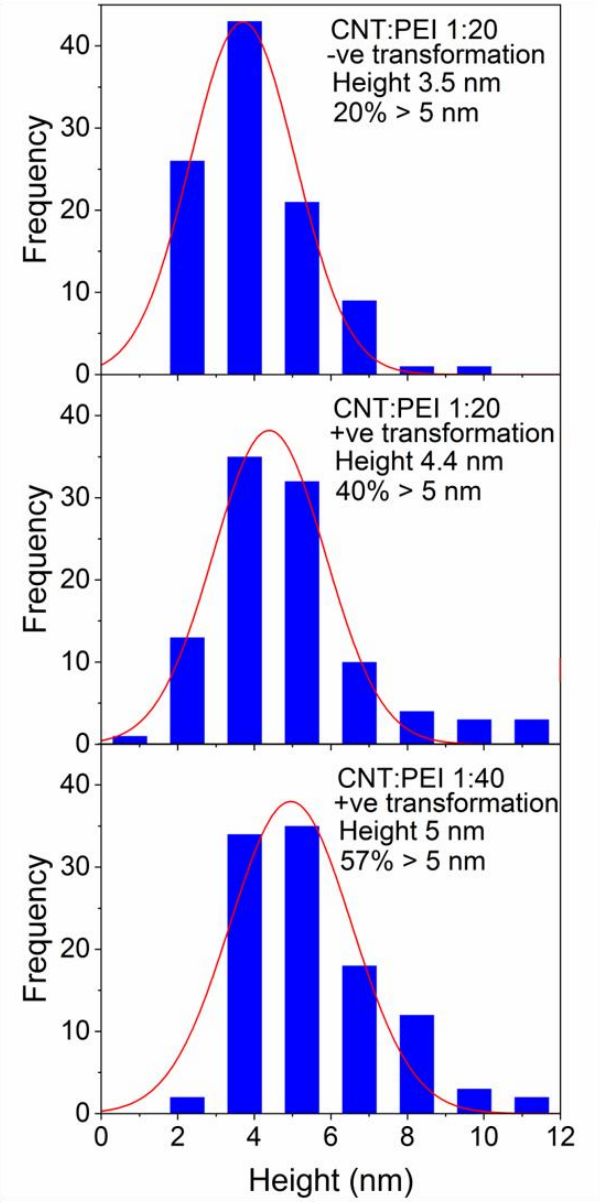
CNT:PEI 1:20
-ve transformation
Height 3.5 nm
20% > 5 nm
CNT:PEI 1:20
+ve transformation
Height 4.4 nm
40% > 5 nm
CNT:PEI 1:40
+ve transformation
Height 5 nm
57% > 5 nm
Frequency
Height (nm)

B

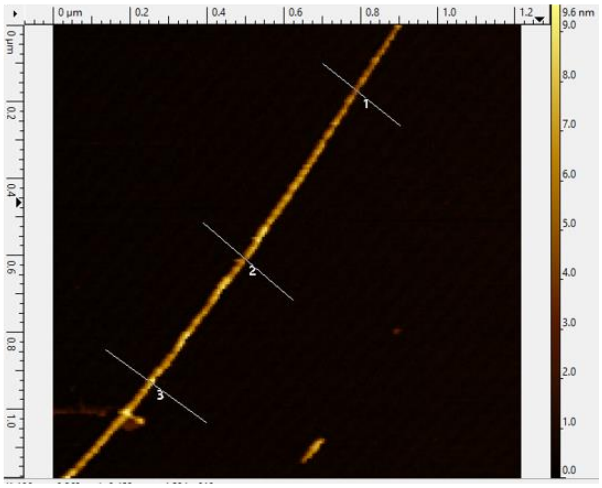

C

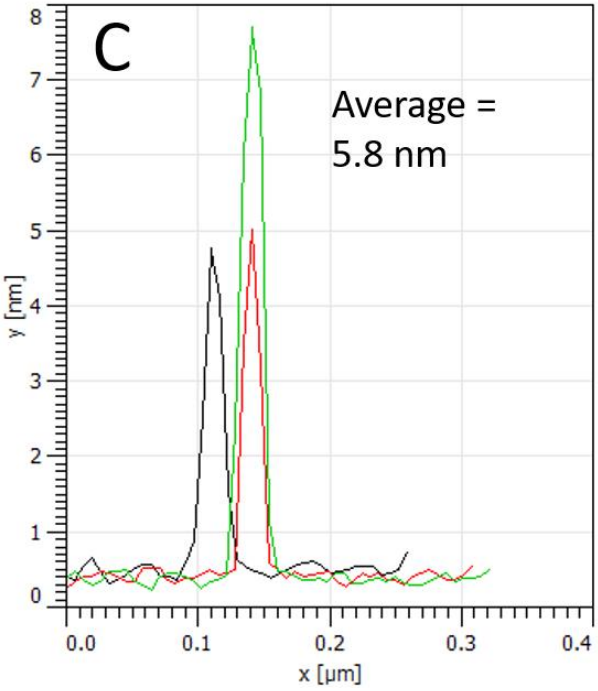
Average =
5.8 nm
y [nm]
x [µm]

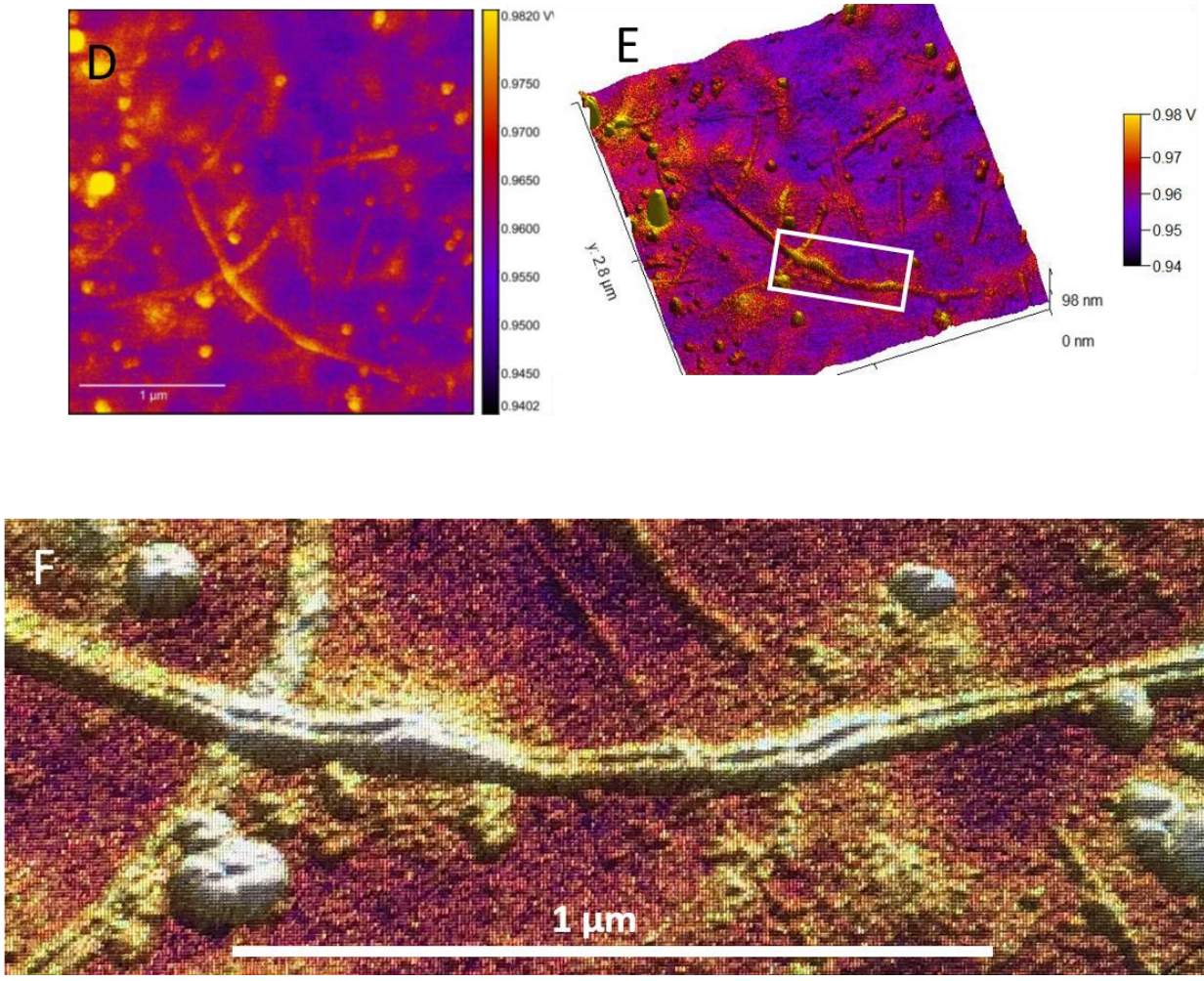

Figure S10. AFM height and work function distribution of different preparations of PEI-SWCNTs. A) AFM height distribution of PEI_{20}-$SWCNT^{+52mV}$, PEI_{20}-$SWCNT^{+61mV}$ and PEI_{40}-$SWCNT^{+77mV}$. B) Dry-phase AFM topographic images of PEI_{40}-$SWCNT^{+77mV}$. The height profile along three perpendicular lines to the tube were recorded and the average was calculated for each tube. C) Height profile of PEI-SWCNT along the lines shown in B. D) and E) 2D and 3D rendering of a representative PEI_{30}-$SWCNT^{+61mV}$: work-function, in color scale, shows the correlation between coating thickness and electrical properties. F) Enlarged view of the rectangular box shown in E.

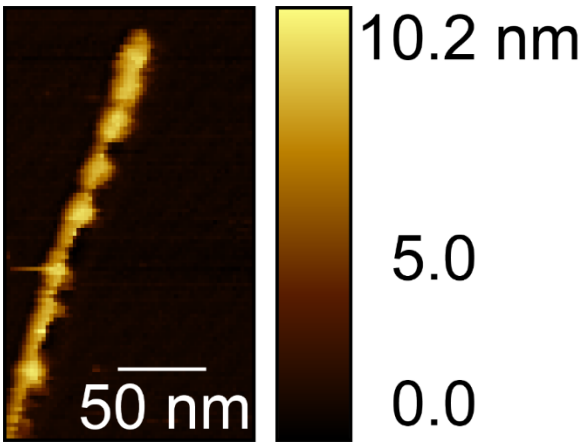

Figure S11. Dry-phase AFM topographic image of $PEI_{0.1}$-$SWCNT^{+30mV}$.

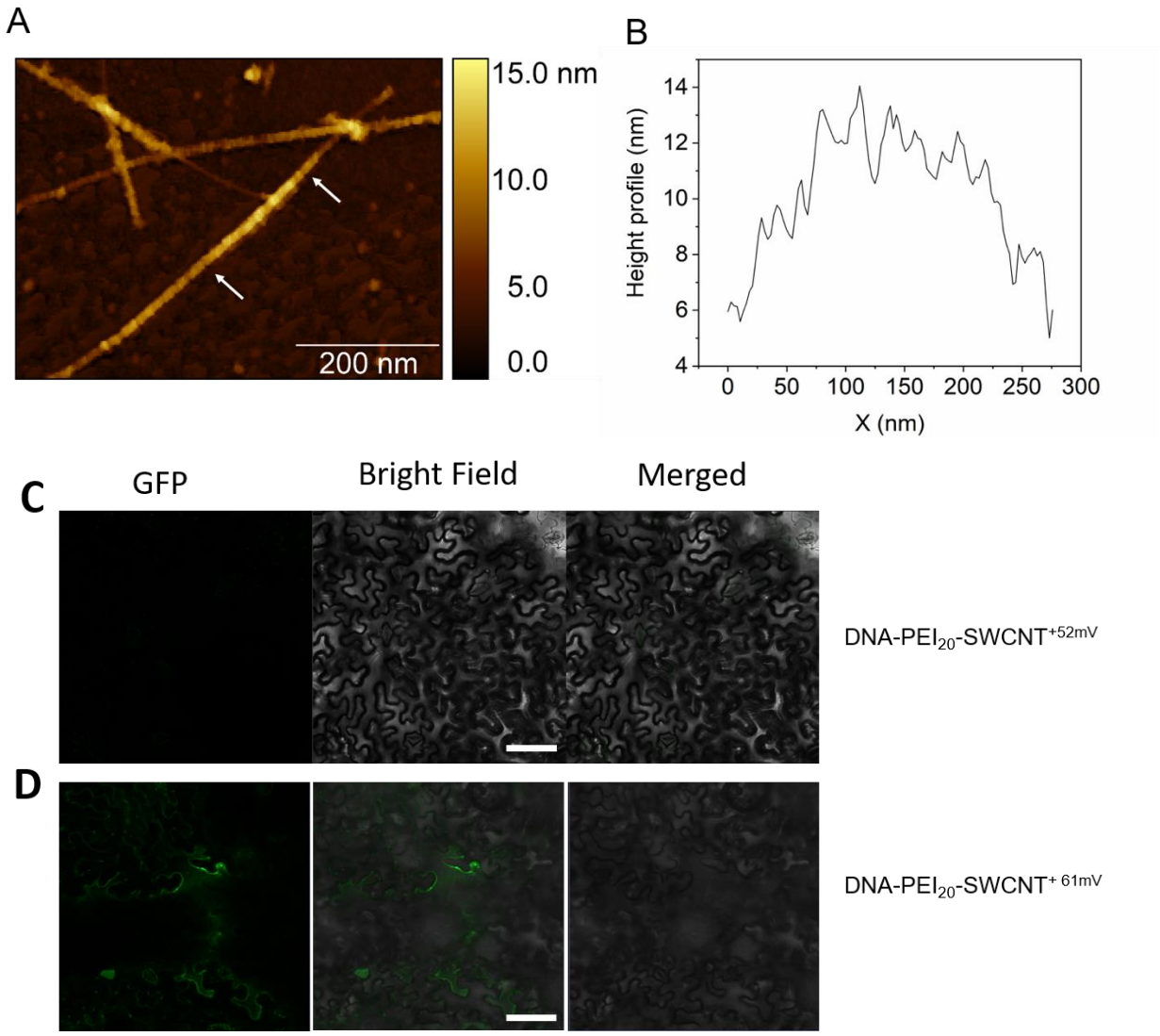

Figure S12. A) Dry-phase AFM topographic image of PEI_{30}-$SWCNT^{+55mV}$ complexed with DNA. The arrows indicate both ends of DNA extended along the surface of the PEI-SWCNT. The height profile (solid plot) between the two arrows is shown in B. This composite failed to show positive GFP expression. B) Height profile of the composite shown in A. C) Confocal microscope images of *N. benthamiana* leaves infiltrated with the TRBO-GFP-PEI_{20}-$SWCNT^{+52mV}$. The infiltrated leaves were subjected to confocal microscopy after 3 days of infiltration. D) Confocal microscope images of *N. benthamiana* leaves infiltrated with the TRBO-GFP-PEI_{20}-$SWCNT^{+61mV}$. Scale bar is 100 μm.

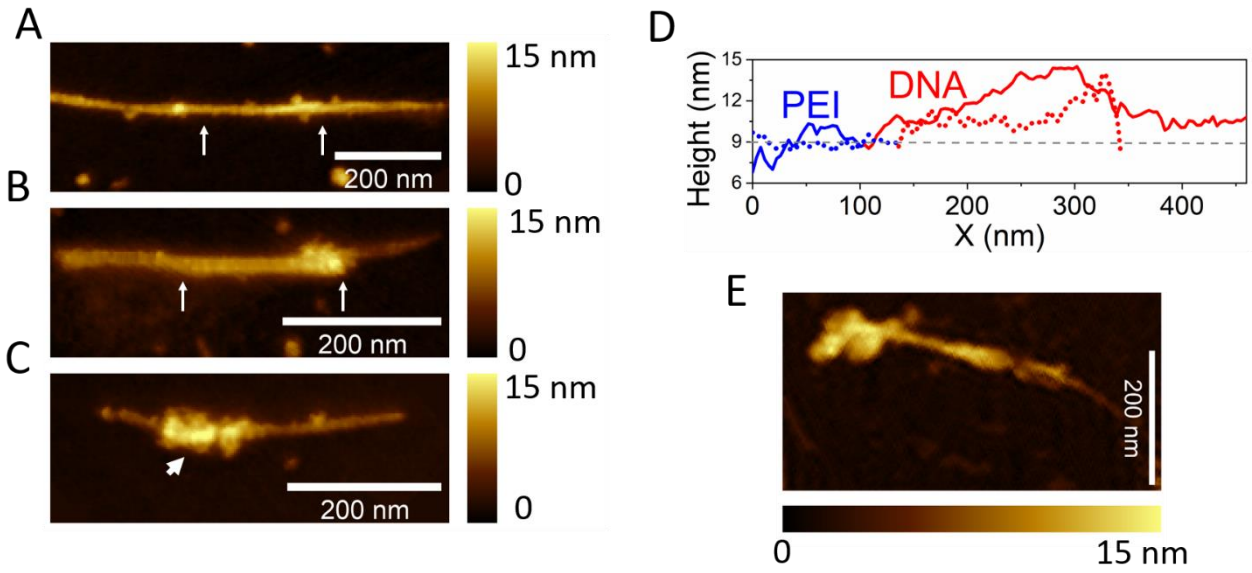

Figure S13. A) Dry-phase AFM topographic image of PEI_{20}-$SWCNT^{+52mV}$. The arrows indicate both ends of DNA extended along the surface of the PEI-SWCNT. The height profile (solid plot) between the two arrows is shown in D. This composite failed to show positive GFP expression (Fig. S12c). B) Dry-phase AFM topographic image of PEI_{30}-$SWCNT_{+61mV}$. The arrows indicate both ends of DNA partially condensed on the surface of the PEI-SWCNT. The height profile (dotted plot) between the two arrows is shown in D. This composite showed positive GFP expression (Fig. 1c). C) Dry-phase AFM topographic image of PEI_{40}-$SWCNT^{+77mV}$. The arrows indicate partially condensed DNA. This composite showed positive GFP expression. D) Height profile of the PEI-SWCNT shown in A, B. E) Dry-phase AFM topographic image of PEI_{20} $SWCNT^{+61mV}$.

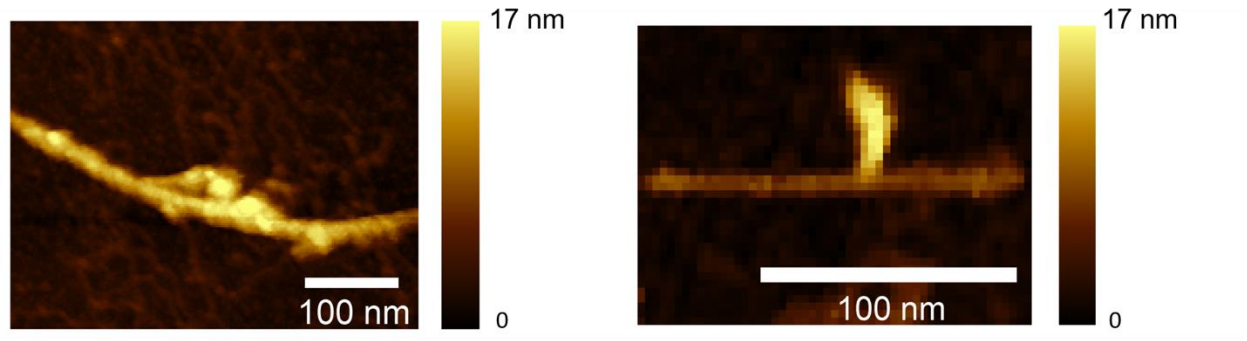

Figure S14. Liquid-phase AFM topographic image of a partially condensed TRBO DNA-PEI_{30}-$SWCNT^{+61mV}$ complex (see Materials and Methods).

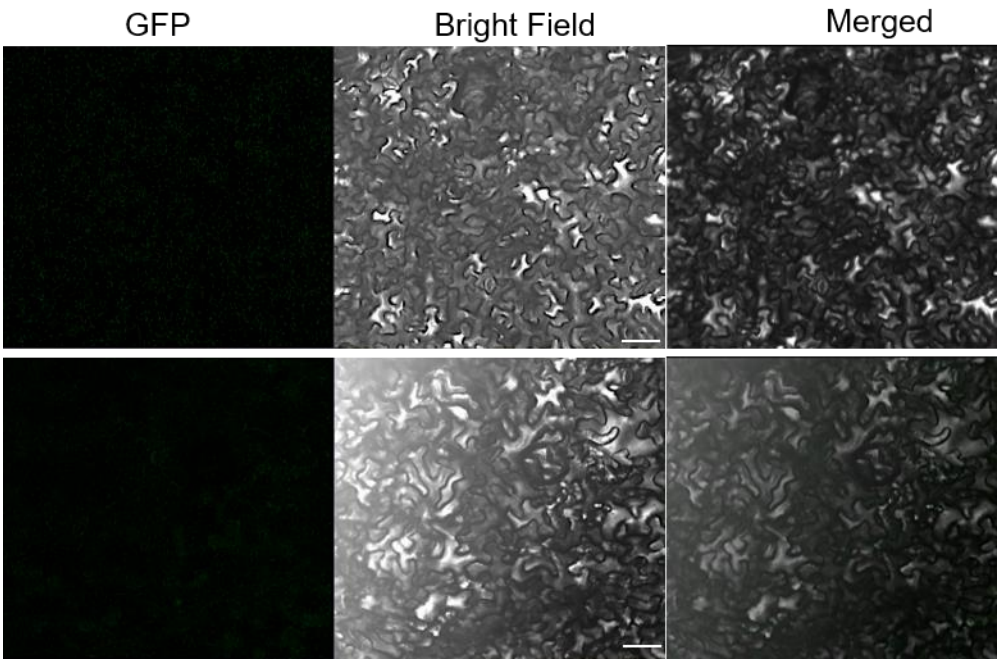

Figure S15. Confocal microscope images of the leaves infiltrated with the $PEI_{0.1}$-SWCNT-TRBO-G complex. The infiltrated leaves were subjected to confocal microscopy after 3 - 5 days of infiltration All images are of 20x magnification, scale bar 100 μm.

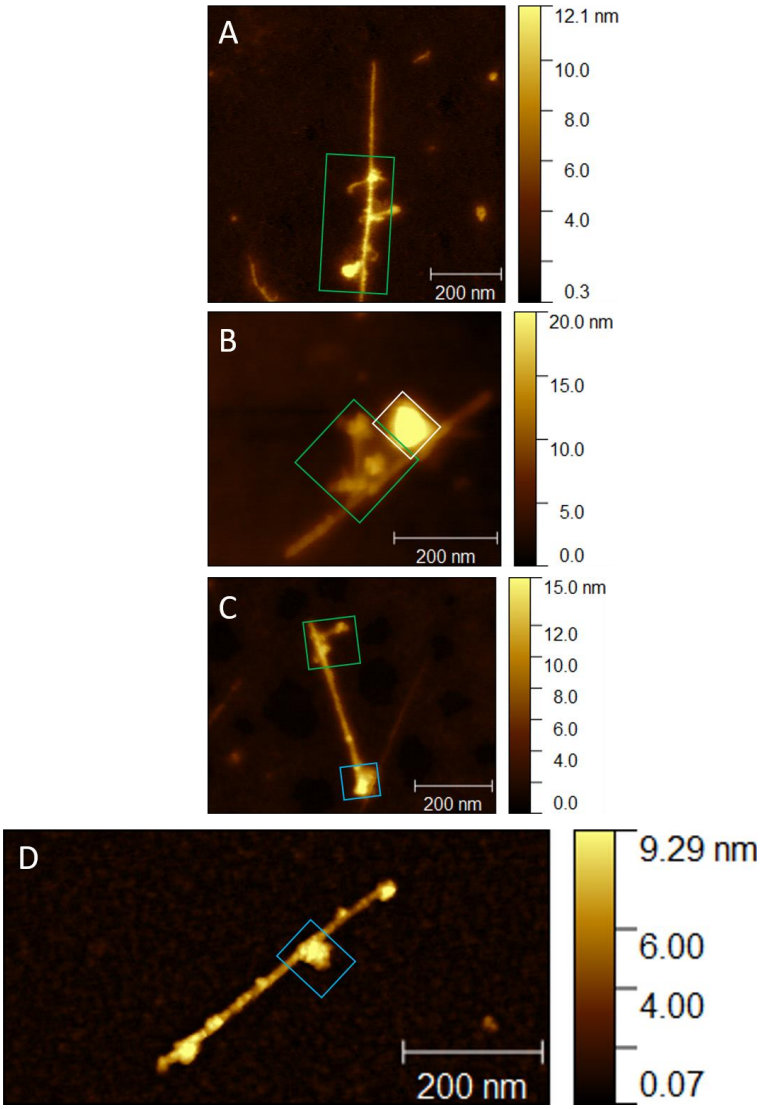

Figure S16. Dry-phase AFM topographic imaging of partially condensed and condensed TRBO DNA on the surface of the PEI_{30}-$SWCNT^{+61}$. The extended mode of binding was identified by following the method described in reference 26 and shown in Fig. 5f, whereas the condensed DNA (Fig. S16D, blue square) was distinguished from the artifacts (Fig. S16B, white square) by the method described in Supplementary text 1. The partially condensed mode of binding was identified *via* the presence of lobes of DNA extruded from the condensed DNA (Fig. S16 A-C, green squares).

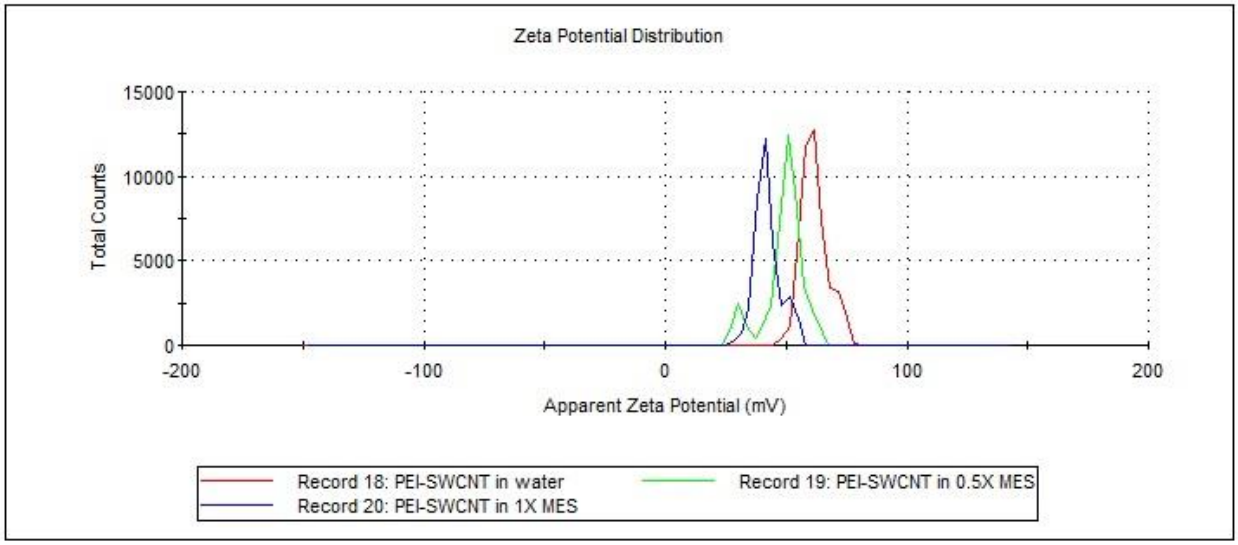

Figure S17. Zeta potential measurements of PEI_{30}-$SWCNT^{+61mV}$ in water, 0.5X MES buffer and 1X MES buffer.

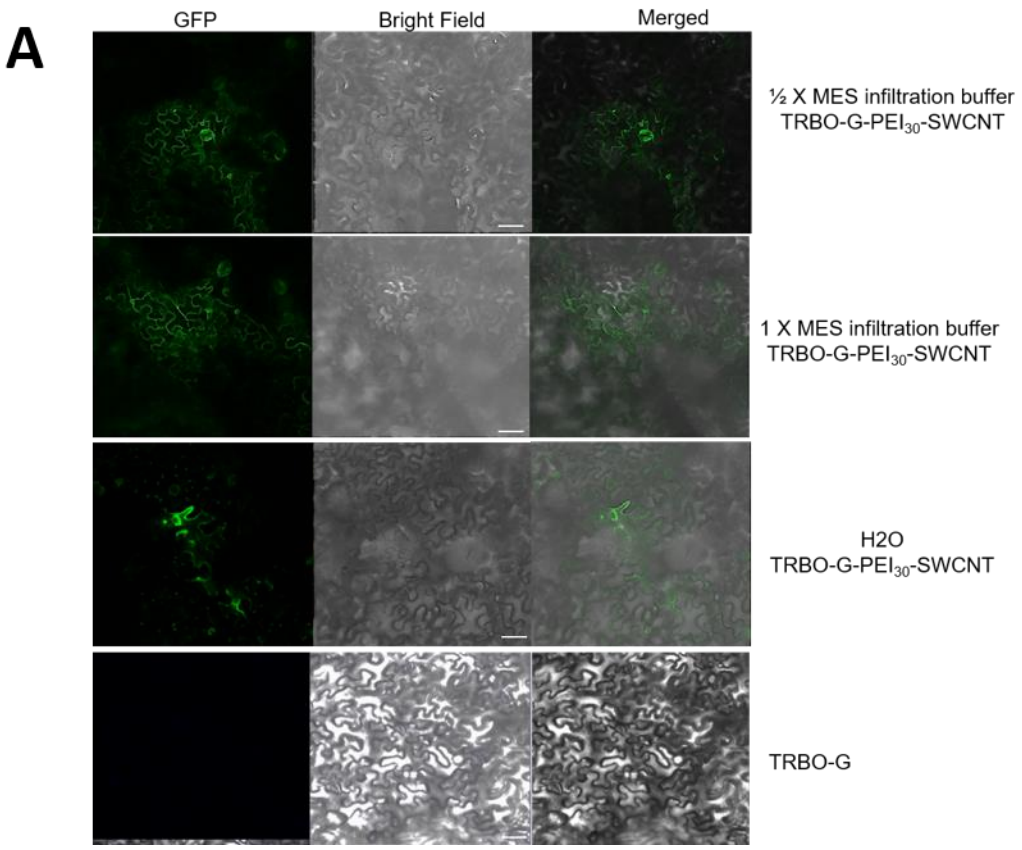
A
GFP
Bright Field
Merged
½ X MES infiltration buffer
TRBO-G-PEI30-SWCNT
1 X MES infiltration buffer
TRBO-G-PEI30-SWCNT
H2O
TRBO-G-PEI30-SWCNT
TRBO-G

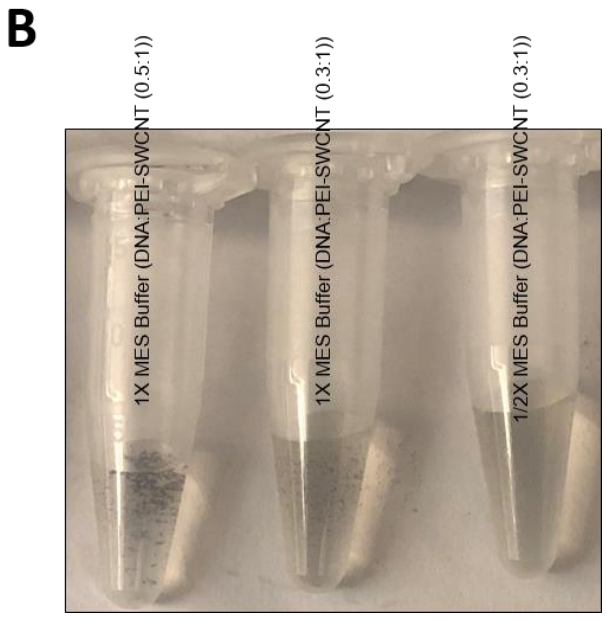
B
1X MES Buffer (DNA:PEI-SWCNT (0.5:1))
1X MES Buffer (DNA:PEI-SWCNT (0.3:1))
1/2X MES Buffer (DNA:PEI-SWCNT (0.3:1))

Figure S18. A) Confocal microscope images of the leaves infiltrated with the TRBO-G-PEI_{30}-$SWCNT^{+61mV}$. TRBO-G-PEI_{30}-$SWCNT^{+61mV}$ were infiltrated to *N. benthamiana* in MES, ½ MES buffer and H_20. The infiltrated leaves were subjected to confocal microscopy after 3 days of infiltration All images are of 20x magnification, scale bar 100 μm. B) Effect of salt concentration (1X MES buffer ($MgCl_2$ (15 mM), MES (25 mM) and ½X MES buffer ($MgCl_2$ (7.5 mM), MES (12.5 mM)) on the aggregation and subsequent precipitation of TRBO-G-PEI_{30}-$SWCNT^{+61mV}$.

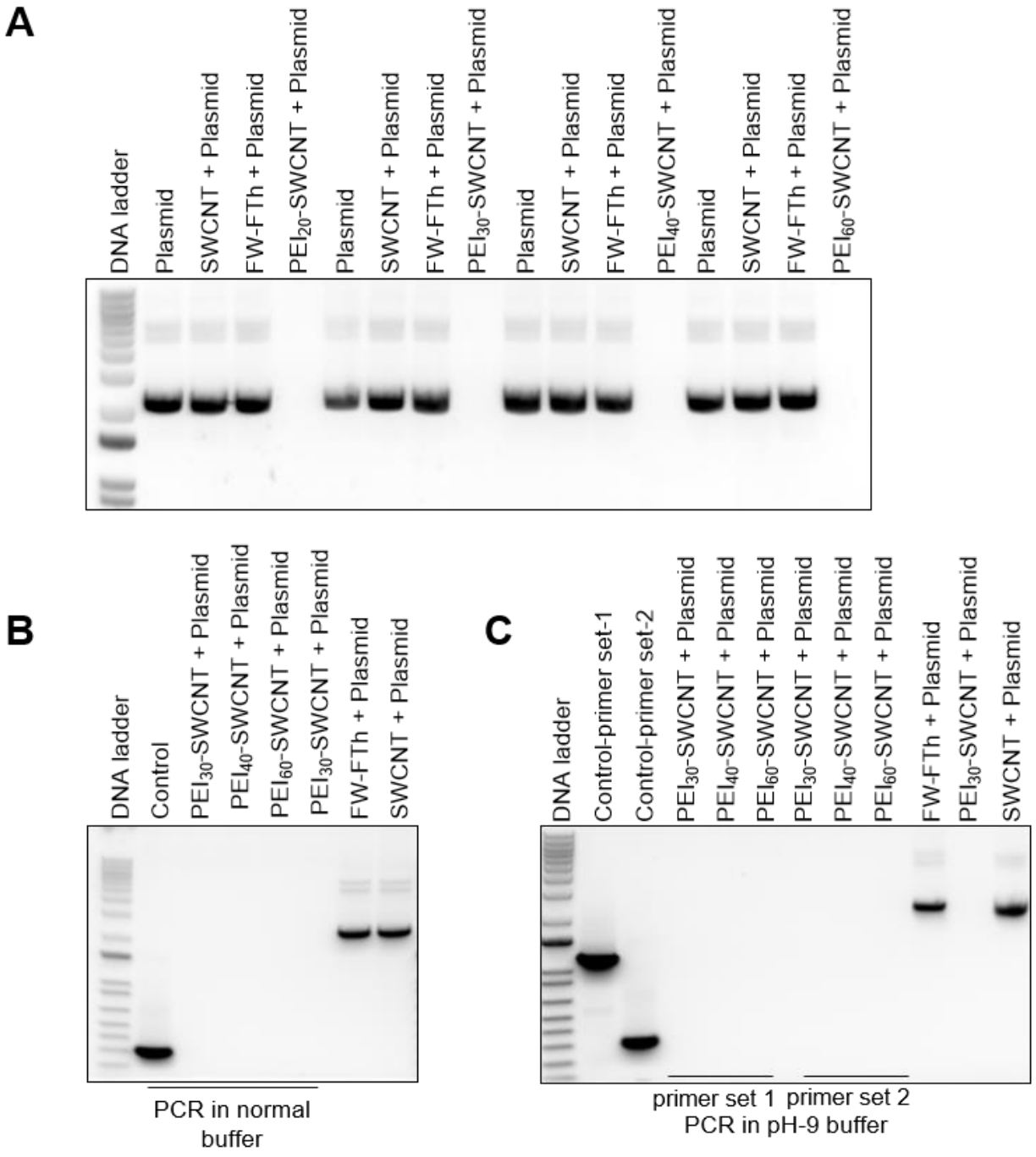

Figure S19. DNA release and availability for processing. A) Plasmid DNA was conjugated with PEI-SWCNTs. DNA-PEI-SWCNT complexes was separated on agarose gel. Plasmid alone, SWCNTs with plasmid, and final wash flow through (FW-FTh) with plasmid were used as control.

B) Availability of the PEI-SWCNT conjugated plasmid for DNA polymerase. Plasmid DNA was conjugated with PEI-SWCNT. DNA-PEI-SWCNT complex was used as template in the PCR reaction in normal PCR buffer. C) Effect of pH. PEI_{30}-SWCNT, PEI_{40}-SWCNT and PEI_{60}-SWCNT and complexes were used as template in the PCR reaction with two different sets of PCR primers in buffer pH9. In B and C, plasmid alone was used as amplification positive control. FW-FTh with plasmid is used to confirm the absence of free PEI in the solution. SWCNTs with plasmid is used as for no DNA binding. PEI_{30}-SWCNTs with plasmid was used as control for DNA binding. The PCR product was separated on a 1% agarose gel.

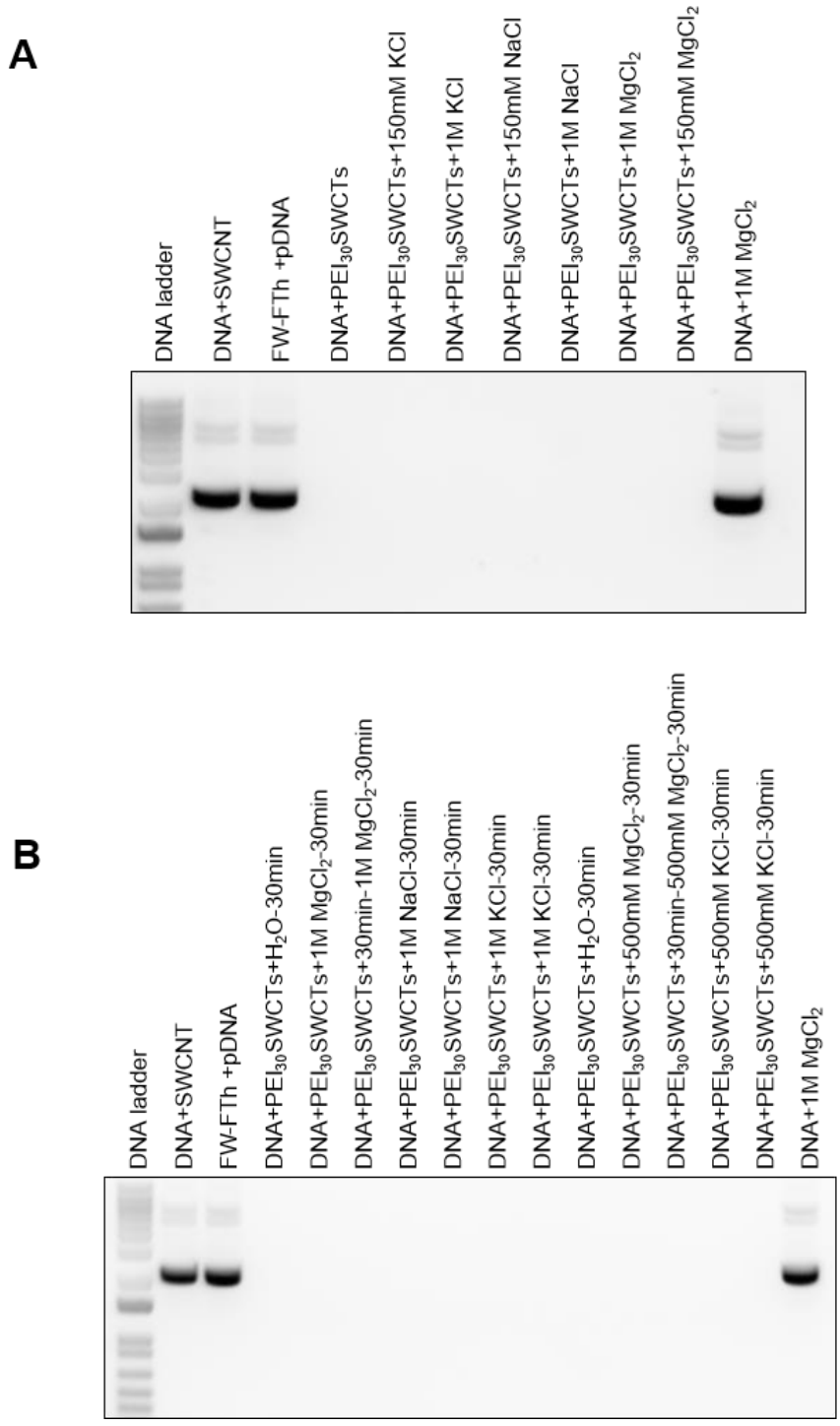

Figure S20. Salt dependent release of plasmid DNA from PEI-SWCNT conjugate. A) PEI-SWCNT-DNA complex were made in the presence of different concentration of KCl, NaCl nd $MgCl_2$ the complex was separated on agarose gel. B) Different concentration of KCl, NaCl and

$MgCl_2$ were added sequentially to make PEI-SWCNT-DNA complex. In A and B, SWCNT with plasmid alone were used as control and final wash flow through (FW-FTh) was used to confirm the absence of free PEI in the solution. The DNA complexes was separated on a 1 % agarose gel.

Supporting Table

Table S1: DNA-PEI-SWCNT complex formation, infiltration and observations

No	Tip-Probe used	PEI Concentration used	No of plants infiltrated	Infiltration in to different spot of the same leaves	Infiltration in to different leaves	Toxicity observation	Confocal results	DNA Condensation status	Consistency in expression	Infiltration butter used	Confirmation by UV	Confirmation by Western blot
1	9mm	1:70	36	no	yes	Observed Toxicity	No expression	Extended	no	pH6 (25mM MES+15mM MgCl2)	no	NA
2	6mm	1:70	36	no	yes	Observed Toxicity	No expression	Extended	no	pH6 (25mM MES+15mM MgCl2)	no	NA
3	6mm	1:40	36	yes	yes	Observed some Toxicity	Observed some expression	condensed	no	pH6 (25mM MES+15mM MgCl2)	no	NA
4	6mm	1:20	36	yes	yes	Observed low Toxicity	Observed some expression	condensed	no	pH6 (25mM MES+15mM MgCl2)	no	NA
5	6mm	1:20	36	yes	yes	Observed low Toxicity	Observed some expression	condensed	no	pH6 (25mM MES+15mM MgCl2)	no	NA
6	6mm	1:30	36	yes	yes	Observed low Toxicity	No expression	Extended	no	pH6 (25mM MES+15mM MgCl2)	no	NA
7	6mm	1:40	36	yes	yes	Observed Toxicity	Observed expression	condensed	no	pH6 (25mM MES+15mM MgCl2)	no	NA
8	6mm	1:20	36	yes	yes	Observed low Toxicity	Observed expression	condensed	no	pH6 (12.5mM MES+7.5mM MgCl2)	no	no
9	6mm	1:30	36	yes	yes	Observed low Toxicity	Observed 2x expression	condensed	no	pH6 (12.5mM MES+7.5mM MgCl2)	no	no
10	6mm	1:40	36	yes	yes	Observed Toxicity	Observed expression	condensed	no	pH6 (12.5mM MES+7.5mM MgCl2)	no	no
11	6mm	1:20	36	yes	yes	Observed low Toxicity	Observed expression	condensed	no	pH6 (12.5mM MES+7.5mM MgCl2) Sequential addition of the buffer	no	no
12	6mm	1:30	36	yes	yes	Observed low Toxicity	Observed 2x expression	condensed	no	pH6 (12.5mM MES+7.5mM MgCl2) Sequential addition of the buffer	no	no
13	6mm	1:40	36	yes	yes	Observed Toxicity	Observed expression	condensed	no	pH6 (12.5mM MES+7.5mM MgCl2) Sequential addition of the buffer	no	no
14	6mm	1:20	36	yes	yes	Observed low Toxicity	Observed expression	condensed	no	pH6 (12.5mM MES+7.5mM MgCl2) H2O, 5 mM KCl, 10 mM KCl	no	no
15	6mm	1:30	36	yes	yes	Observed low Toxicity	Observed 2x expression	condensed	consistent	pH6 (12.5mM MES+7.5mM MgCl2) H2O, 5 mM KCl, 10 mM KCl	no	no
16	6mm	1:40	36	yes	yes	Observed Toxicity	Observed expression	condensed	no	pH6 (12.5mM MES+7.5mM MgCl2) H2O, 5 mM KCl, 10 mM KCl	no	no
17	6mm	1:20	36	yes	yes	Observed low Toxicity	Observed expression	condensed	no	pH6 (12.5mM MES+7.5mM MgCl2)	no	no
18	6mm	1:30	36	yes	yes	Observed low Toxicity	Observed 2x expression	condensed	consistent	pH6 (12.5mM MES+7.5mM MgCl2)	no	no
19	6mm	1:40	36	yes	yes	Observed Toxicity	Observed expression		no	pH6 (12.5mM MES+7.5mM MgCl2)	no	no

Light green: multiple repeats of ½ X infiltration buffer with 1:30 (SWCNT:PEI).

Magenta: 1X infiltration buffer with 1:30 (SWCNT:PEI).

No color: All other combinations with different PEI and infiltration buffers.

Supporting equipment and reagents

Equipment

Scanning Probe Microscope Agilent 5500 (Agilent Technologies, CA, USA)

Silicon nitride tips (AC40, Bruker)

Zeiss LSM 710 Inverted Confocal Microscope

Sterile syringe filter (0.45 μm; VWR, cat. no. 28145-481)

Disposable centrifuge tubes 50 ml (FisherBrand, cat. no. 055396)

Ultrasonic bath (Branson, cat. no. 1800)

Ultrasonic homogenizer with 6-mm tip (Cole-Parmer, cat. nos. UX-04711-70 and UX-04712-14)

Vortex mixer (Fisher Scientific, cat. no. 02-215-365)

pH meter (accumet AB150)

100,000-MWCO filter units (Amicon, cat. no. UFC910024)

Visible spectrophotometer (Hitachi)

centrifuge (Eppendorf, cat. no. 5424)

Tabletop centrifuge (Eppendorf, cat. no. 5810)

Dynamic light-scattering instrument (Zetasizer Nano ZS; Malvern Instruments)

Folded capillary zeta cell (Malvern Instruments, cat. no. DTS1070)

Microscope cover glass (no. 1; Fisher Scientific, cat. no. 12-542B)

Microscope slides (VWR, cat. no. 16004-422)

Syringe (1 mL; BD, cat. no. 14-823-434)

Chemicals, reagents, and useable

Pure Yield plasmid miniprep system (Promega cat. no. A1222)

Pure Yield plasmid maxiprep system (Promega cat. no. A2393)

Wizard sv Gel and PCR cleanup system ((Promega cat. no. A9282)

Carbon nanotubes (single-walled, carboxylic acid functionalized; Sigma-Aldrich, cat. no. 652490)

Polyethylenimine (PEI, branched, molecular weight (MW) 25,000; Sigma-Aldrich, cat. no. 408727)

MES hydrate (Sigma-Aldrich, cat. no. M5287)

N-(3-dimethylaminopropyl)-*N*′-ethylcarbodiimide hydrochloride (EDC; Sigma-Aldrich, cat. no. E1769)

N-hydroxysulfosuccinimide sodium salt (NHS; Sigma-Aldrich, cat. no. 106627-54-7)

Nuclease-free water (Qiagen, cat. no. 129114)

10× PBS (Corning, cat. no. 46-013-CM)

Hydrochloric acid (HCl, 37% (vol/vol); Sigma-Aldrich, cat. no. 320331)

Sodium hydroxide (NaOH; Sigma-Aldrich, cat. no. S8045)

Magnesium chloride hexahydrate ($MgCl_2.6H_20$; Sigma-Aldrich, cat. no. M2670)

iTaq universal SYBER Green One Step kit (catalog number 1725150, BioRad)

DirectZol (RNA miniprep kit (ZymoResearch, cat. no. R2072)

myTXTL Kit, (Arbor Biosciences)

Templiphi^{TM} 100 Amplification kit (catalog number 25640010, GE Health Care)

RNeasy Plant Mini Kit (Qiagen, cat. no. 74904)

TRBO-GFP qPCR-F CCAGACAACCATTACCTGTCG

TRBO-GFP qPCR-R GCTCATCCATGCCATGTGTA

PP2A-F GACCCTGATGTTGATGTTCGCT

PP2A-R GAGGGATTTGAAGAGAGATTTC

Tris–HCl (Sigma, cat. no. T5941-100G)

NaCl (Sigma, cat. no. S7653-1KG)

Supporting Appendix

1. AFM topographic views of PEI_{20}-$SWCNT^{+52mV}$.

This composite did not show expression in *N. benthamiana* cells (Fig. S12c). Scale bars: 200 nm.

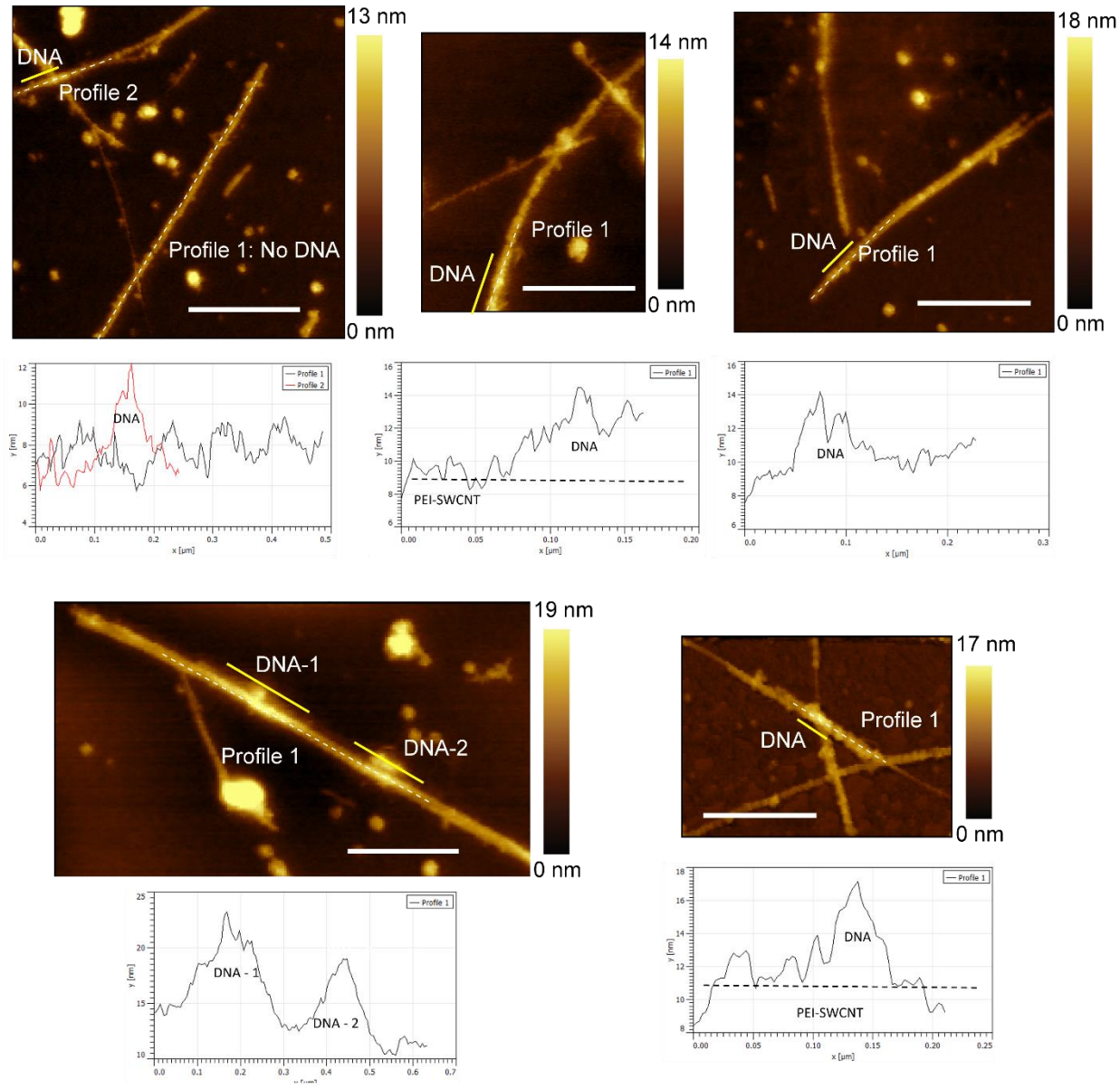

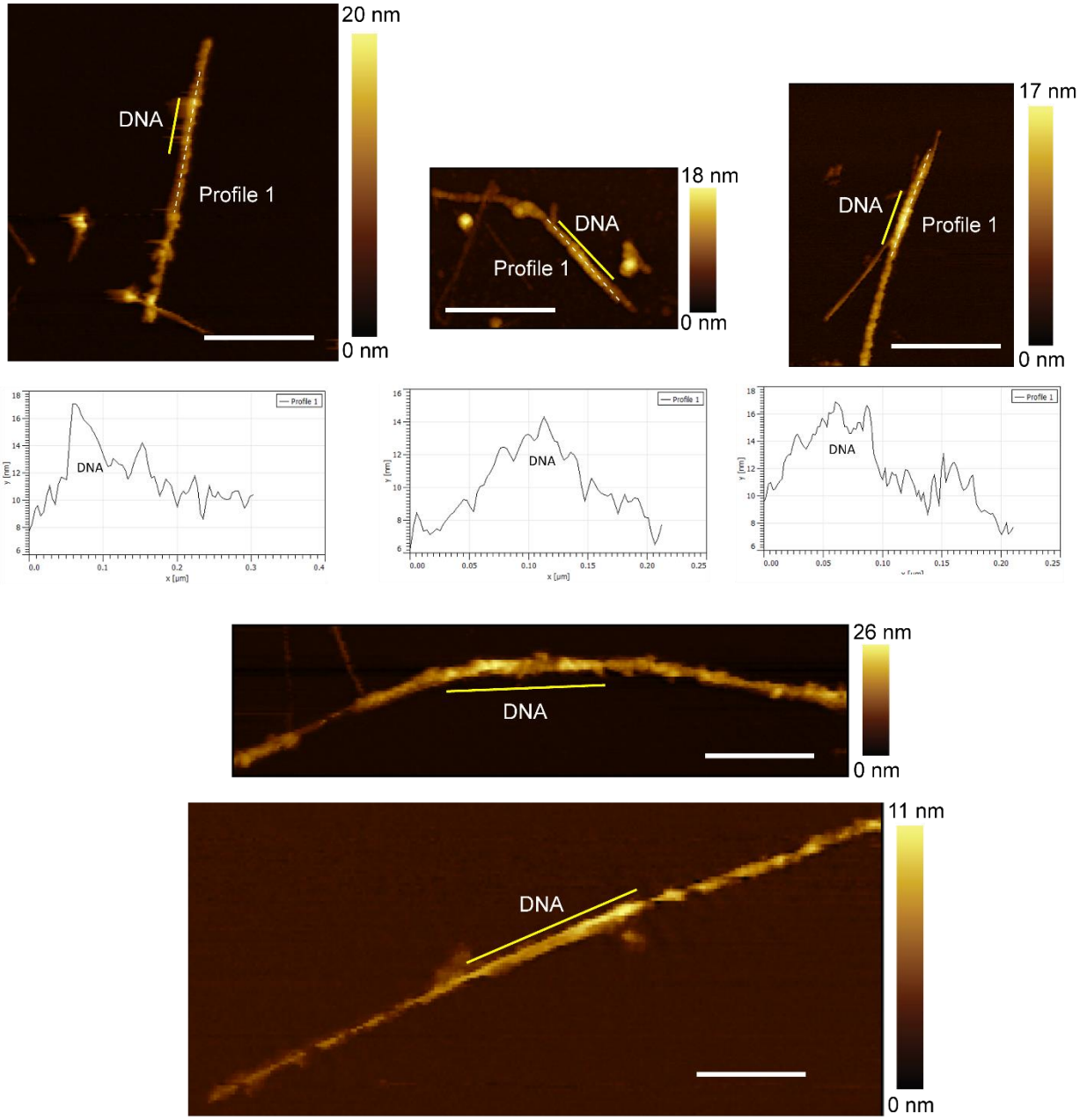
20 nm
DNA
Profile 1
0 nm
18 nm
DNA
Profile 1
0 nm
17 nm
DNA
Profile 1
0 nm
Profile 1
DNA
y [nm]
x [µm]
Profile 1
DNA
y [nm]
x [µm]
Profile 1
DNA
y [nm]
26 nm
DNA
0 nm
11 nm
DNA
0 nm

2. AFM topographic views of PEI_{20}-$SWCNT^{+61mV}$.

This composite showed expression in *N. benthamiana cells* (Fig. S12d). Scale bars: 500 nm.

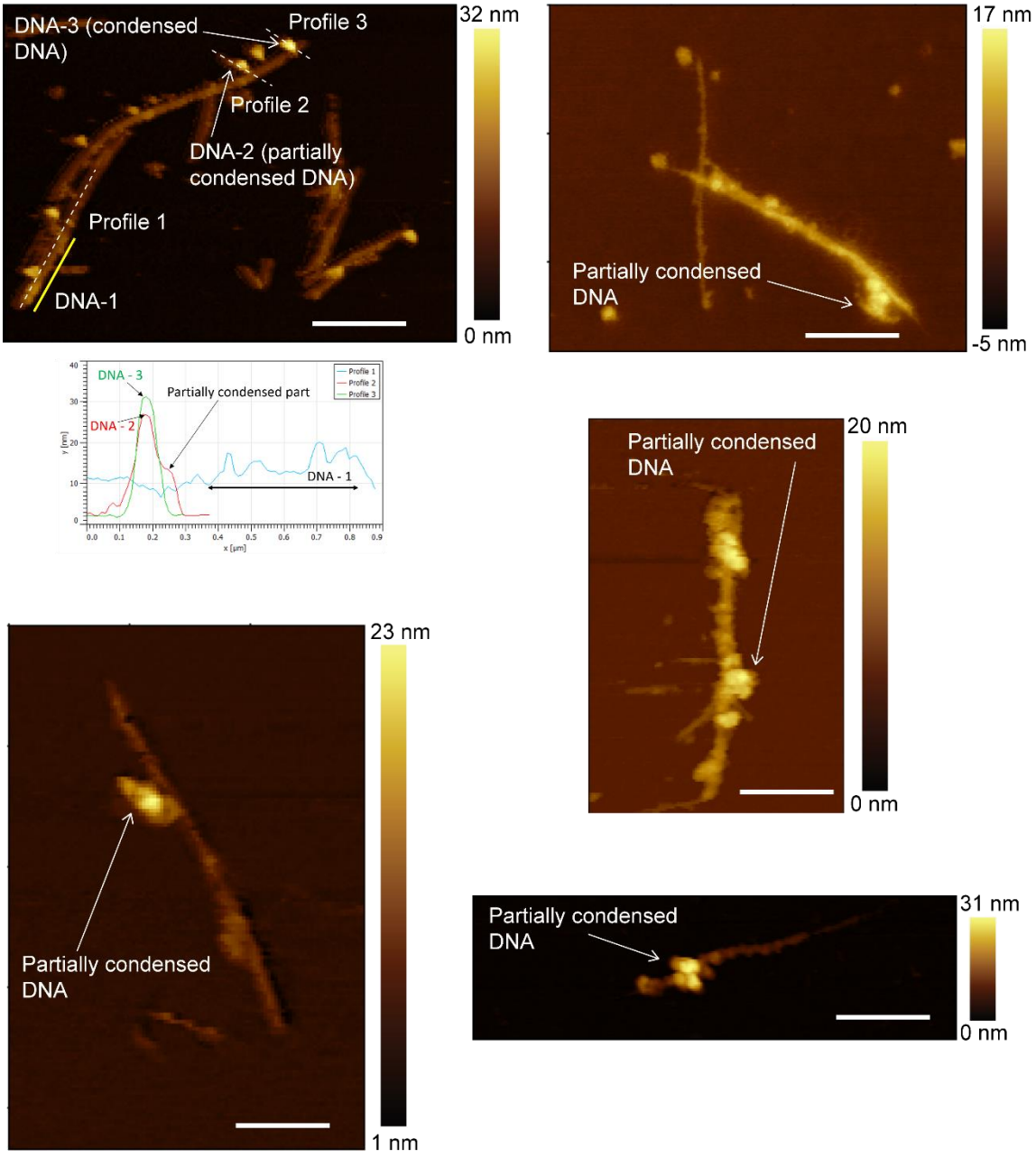

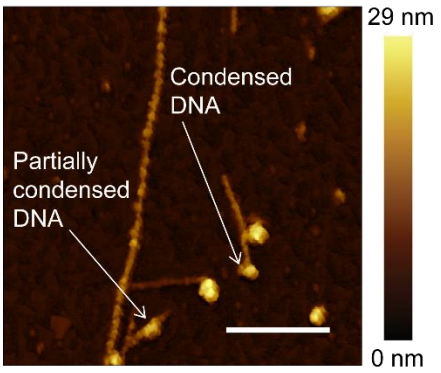
29 nm
Condensed DNA
Partially condensed DNA
0 nm

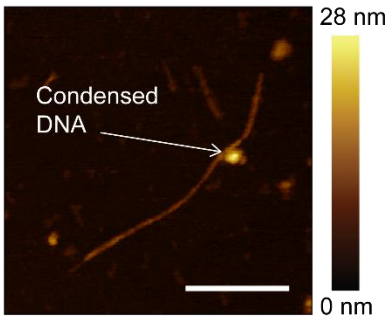
28 nm
Condensed DNA
0 nm

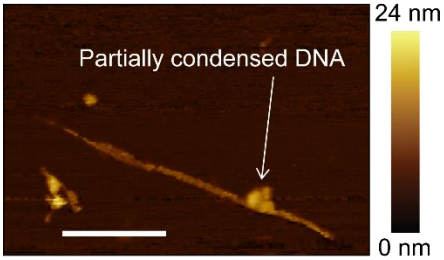
24 nm
Partially condensed DNA
0 nm

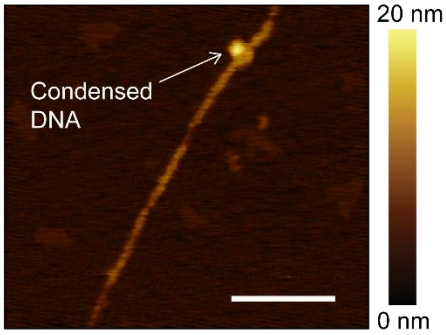
20 nm
Condensed DNA
0 nm

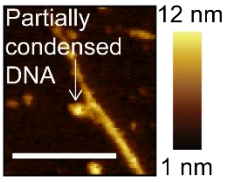
Partially condensed DNA
12 nm
1 nm

Maps of the plasmids used in this study.

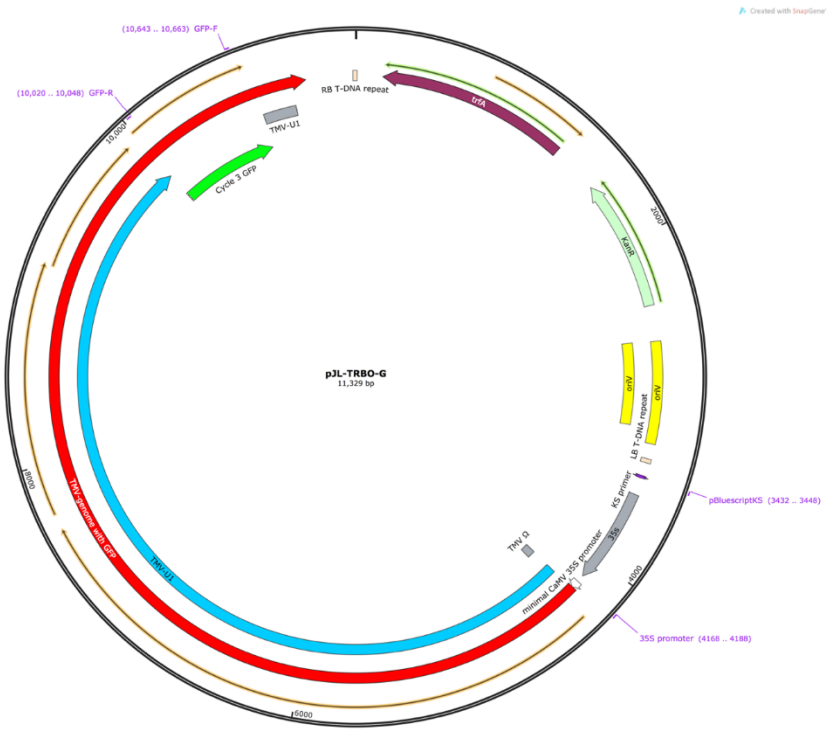

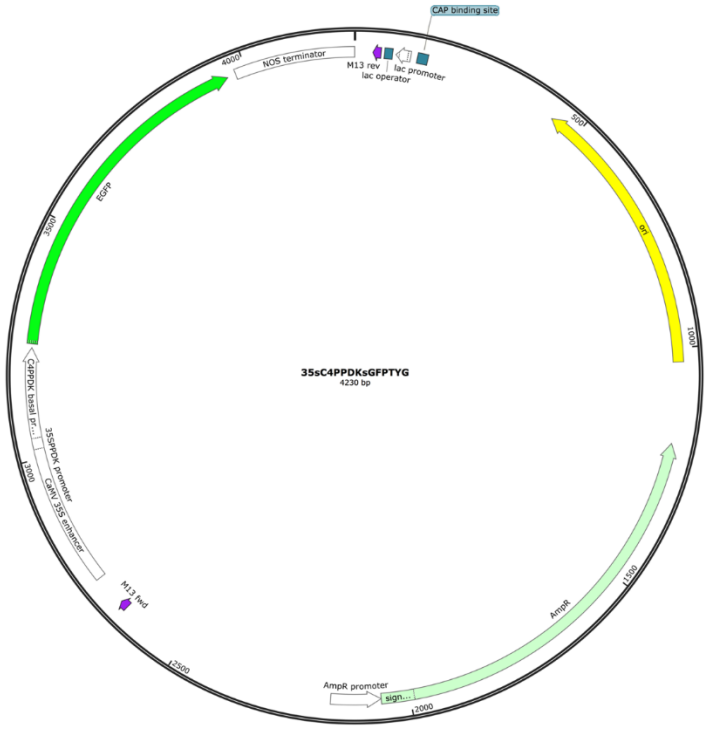

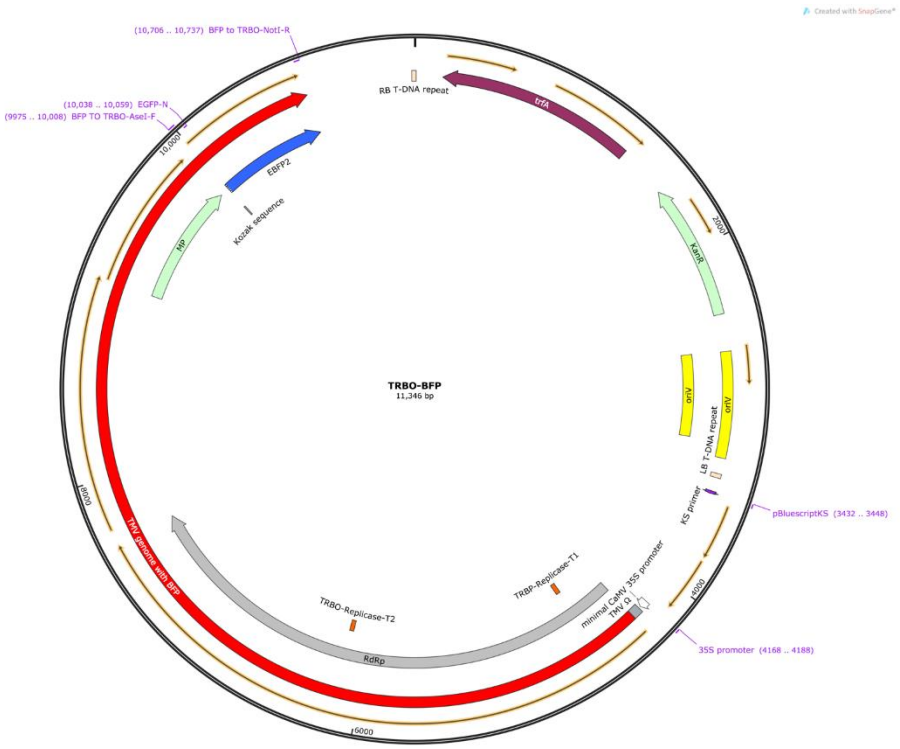
Created with SnapGene®
(10,706 .. 10,737) BFP to TRBO-NotI-R
(10,038 .. 10,059) EGFP-N
(9975 .. 10,008) BFP TO TRBO-AseI-F
RB T-DNA repeat
trfA
EBFP2
Kozak sequence
NP
KanR
oriV
oriV
LB T-DNA repeat
KS primer
pBluescriptKS (3432 .. 3448)
TRBO-BFP
11,346 bp
TRBP-Replicase-T1
minimal CaMV 35S promoter
TMV Ω
TRBO-Replicase-T2
RdRp
35S promoter (4168 .. 4188)
1kb rewrote with BFP
1000
2000
3000
4000
5000
6000
7000
8000
9000
10,000

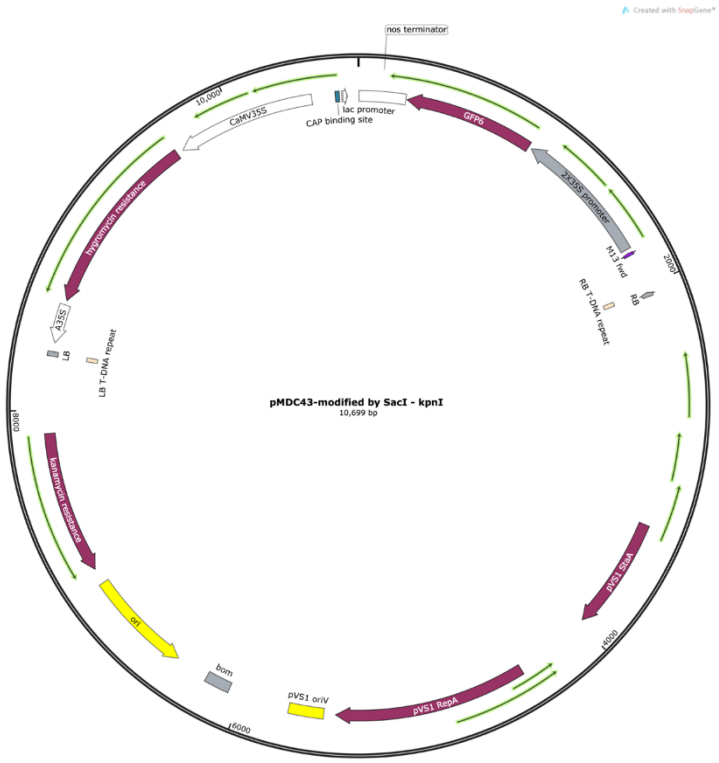
Created with SnapGene®
nos terminator
10,000
CaMV35S
lac promoter
CAP binding site
GFP6
2x35S promoter
M13 fwd
RB
RB T-DNA repeat
Streptomycin resistance
35S
LB
LB T-DNA repeat
pVS1 StbA
pVS1 RepA
pVS1 oriV
bom
ori
Kanamycin resistance
pMDC43-modified by SacI - kpnI
10,699 bp
1000
2000
3000
4000
5000
6000
7000
8000
9000

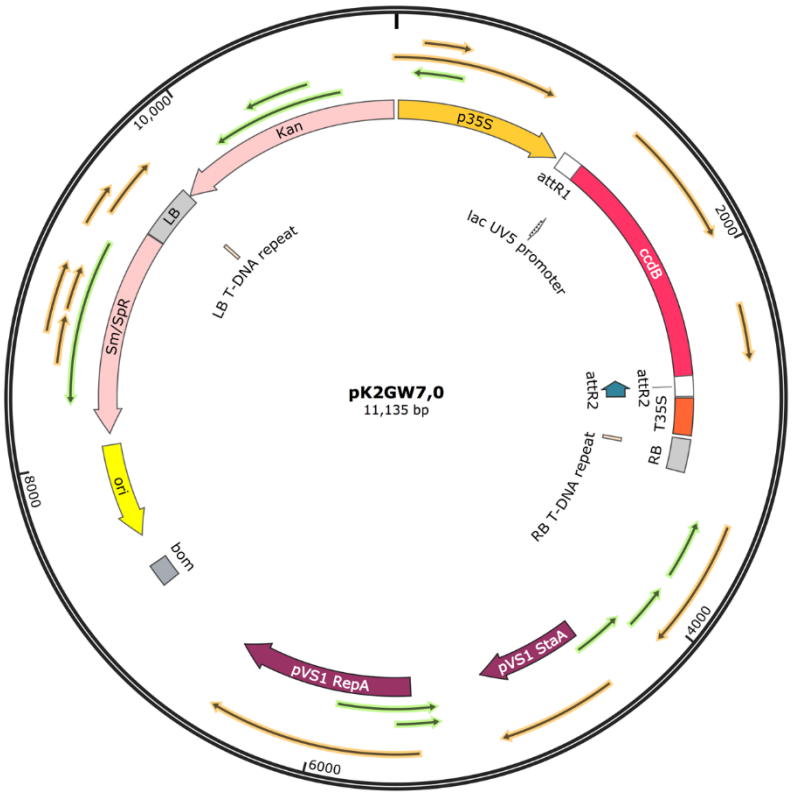
Created with SnapGene®
pK2GW7,0
11,135 bp
10,000
2000
4000
6000
8000
Kan
p35S
attR1
ccdB
attR2
T35S
RB
RB T-DNA repeat
lac UV5 promoter
LB T-DNA repeat
LB
Sm/SpR
ori
bom
pVS1 RepA
pVS1 StaA

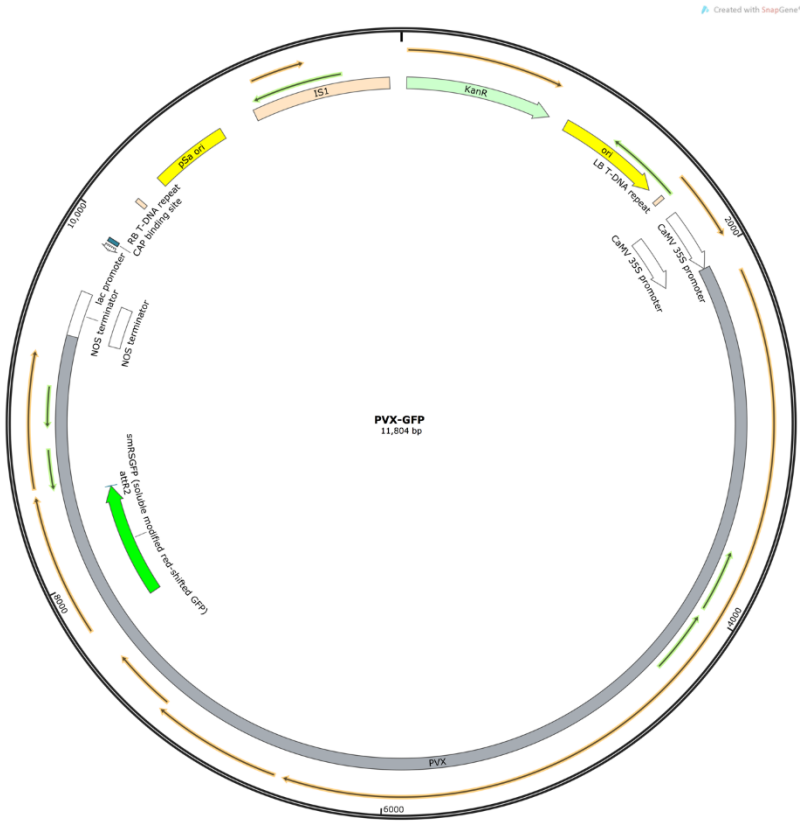
Created with SnapGene®
PVX-GFP
11,804 bp
10,000
2000
4000
6000
8000
IS1
KanR
pSa ori
ori
LB T-DNA repeat
RB T-DNA repeat
CAB binding site
lac promoter
NOS terminator
NOS terminator
CaMV 35S promoter
CaMV 35S promoter
attR2
smRSGFP (soluble modified red-shifted GFP)
PVX


Created with SnapGene®
pK2GW7-TYLCV
12,919 bp
p35S
attB1
attB1
TYLCV-2 infectious clone
attB2
attB2
RB T-DNA repeat
RB
nos
pVS1 RepA
pVS1 StaA
ori
bom
SmSpR
LB
LB T-DNA repeat
NOS terminator
Kan
12,000
2000
4000
6000
8000
10,000

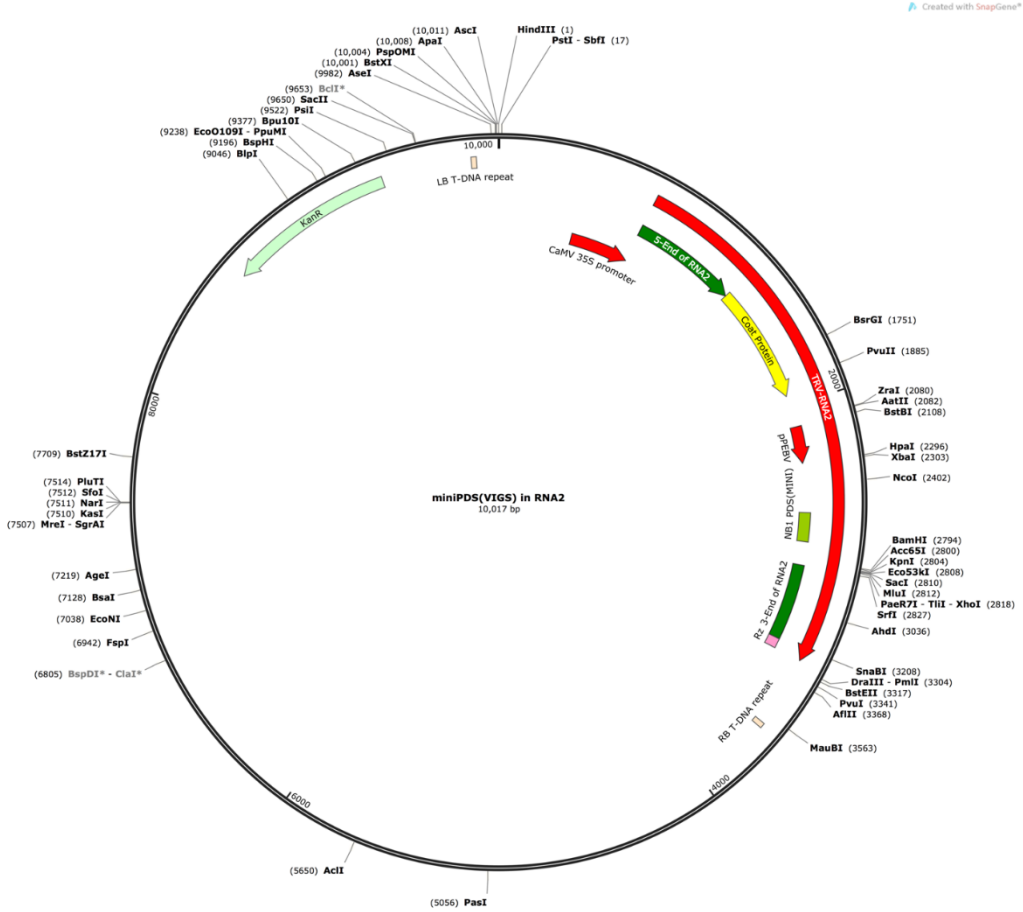
Created with SnapGene®
miniPDS(VIGS) in RNA2
10,017 bp
LB T-DNA repeat
10,000
(10,011) AscI
(10,008) ApaI
(10,004) PspOMI
(10,001) BstXI
(9982) AseI
(9653) BclI*
(9650) SacII
(9522) PsiI
(9377) Bpu10I
(9238) EcoO109I - PpuMI
(9196) BspHI
(9046) BlpI
HindIII (1)
PstI - SbfI (17)
KanR
CaMV 35S promoter
5-End of RNA2
Coat Protein
TNV-RNA2
3'-End of RNA2
NB1 PDS(M1N1)
pPEBV
RB T-DNA repeat
(7709) BstZ17I
(7514) PluTI
(7512) SfoI
(7511) NarI
(7510) KasI
(7507) MreI - SgrAI
(7219) AgeI
(7128) BsaI
(7038) EcoNI
(6942) FspI
(6805) BspDI* - ClaI*
(5650) AclI
(5056) PasI
BsrGI (1751)
PvuII (1885)
ZraI (2080)
AatII (2082)
BstBI (2108)
HpaI (2296)
XbaI (2303)
NcoI (2402)
BamHI (2794)
Acc65I (2800)
KpnI (2804)
Eco53kI (2808)
SacI (2810)
MluI (2812)
PaeR7I - TliI - XhoI (2818)
SrfI (2827)
AhdI (3036)
SnaBI (3208)
DraIII - PmlI (3304)
BstEII (3317)
PvuI (3341)
AflII (3368)
MauBI (3563)
2000
4000
6000
8000

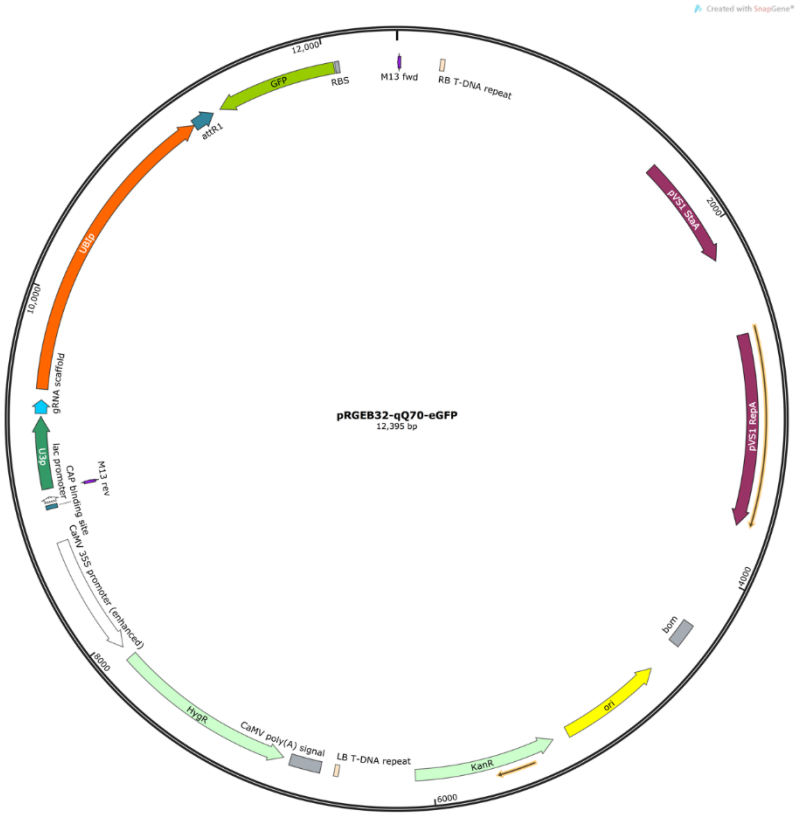
Created with SnapGene®
12,000
GFP
RBS
M13 fwd
RB T-DNA repeat
attR1
LR0
pVS1 StbA
2000
10,000
gRNA scaffold
pVS1 RepA
pRGEB32-qQ70-eGFP
12,395 bp
lac promoter
M13 rev
CAP binding site
CaMV 35S promoter (enhanced)
4000
born
8000
HygR
CaMV poly(A) signal
LB T-DNA repeat
ori
KanR
6000

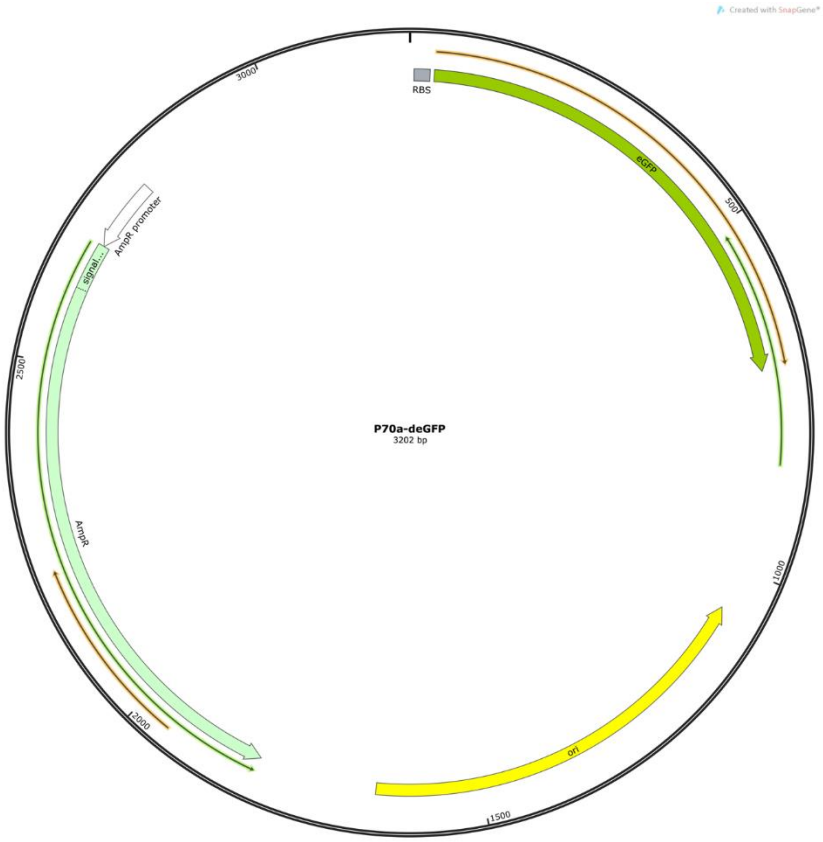
Created with SnapGene®
3000
RBS
egfp
500
AmpR promoter
signal...
2500
P70a-deGFP
3202 bp
AmpR
1000
2000
ori
1500

Supporting References

1- Manning, G. S., Counterion Condensation Theory of Attraction Between Like Charges in the Absence of Multivalent Counterions. *The European physical journal. E, Soft matter* **2011,** *34*, 1-18.